Nonlinear Dyn (2016) 84:1225–1258
DOI 10.1007/s11071-015-2564-5

ORIGINAL PAPER

Nonlinear vibration response analysis of a rotor-blade system with blade-tip rubbing

Hui Ma · Fanli Yin · Zhiyuan Wu · Xingyu Tai · Bangchun Wen

Received: 11 September 2015 / Accepted: 13 December 2015 / Published online: 29 December 2015

Abstract An improved rotor-blade dynamic model is developed based on our previous works (Ma et al. in J Sound Vib, 337:301–320, 2015; J Sound Vib 357:168–194, 2015). In the proposed model, the shaft is discretized using a finite element method and the effects of the swing of the rigid disk and stagger angles of the blades are considered. Furthermore, the mode shapes of rotor-blade systems can be obtained based on the proposed model. The proposed model is more accurate than our previous model, and it is also verified by comparing the natural frequencies obtained from the proposed model with those from the finite element model and published literature. By simplifying the casing as a two degrees of freedom model, the single- and four-blade rubbings are studied using numerical simulation and experiment. Results show that for both the single- and four-blade rubbings, amplitude amplification phenomena can be observed when the multiple frequencies of the rotational frequency (f_r) coincide with the conical and torsional natural frequencies of the rotor-blade system, natural frequencies of the casing and the bending natural frequencies of the blades. In addition, for the four-blade rubbing, the blade passing frequency (BPF, $4f_r$) and its multiple frequency components also have larger amplitudes, especially, when they coincide with the natural frequencies of the rotor-blade system or casing; the four-blade rubbing levels are related to the rotor whirl, and the most severe rubbing happens on the blade located at the right end of the whirl orbit.

Keywords Rotor-blade systems · Blade-tip rubbing · Vibration responses · Amplitude amplification phenomena · Experiment

H. Ma (✉) · F. Yin · Z. Wu
School of Mechanical Engineering and Automation, Northeastern University, Shenyang 110819, Liaoning, People's Republic of China
e-mail: mahui_2007@163.com

X. Tai · B. Wen
Shenyang Blower Works Group Corporation, Shenyang 110869, People's Republic of China

List of symbols

$\boldsymbol{C}_{\mathrm{RB}}$	Viscous damping matrix of the rotor-blade system
$c_{\mathrm{b}X}$, $c_{\mathrm{b}Y}$, $c_{\mathrm{b}Z}$	Bearing damping in X, Y and Z directions
$c_{\mathrm{c}X}$, $c_{\mathrm{c}Y}$	Damping of the casing in X and Y directions
E	Young's modulus of blade
$\boldsymbol{e}_{\mathrm{c}}$	Vector of the eccentricity of the static equilibrium positions of the rotor and casing center line
$\boldsymbol{F}_{\mathrm{c}}$	Rubbing force vector of the casing
$\boldsymbol{F}_{\mathrm{nonlinear},}$, $\boldsymbol{F}_{\mathrm{rub}}$	Nonlinear force and rubbing force vectors of the rotor-blade system

$\boldsymbol{F}_{\text{nonlinear,b}}$, $\boldsymbol{F}_{\text{nonlinear,s}}$	Nonlinear force vectors of the blade and shaft
F_{n}, F_{t}	Normal and tangential rubbing forces
$f_{\text{n}i}$	The ith natural frequency of the rotor-blade system (Hz)
f_{r}	Rotational frequency
G_{b}	Shear modulus of the blade
$\boldsymbol{G}_{\text{b}}$, $\boldsymbol{G}_{\text{d}}$	Coriolis matrices of the blade and disk
$\boldsymbol{G}_{\text{c1}}, \ldots, \boldsymbol{G}_{\text{c6}}$	Coupling terms of damping matrix
$\boldsymbol{G}^{\text{e}}$	Gyroscopic matrix of the Timoshenko beam element
$\boldsymbol{G}_{\text{RB}}$	A matrix including the Coriolis force matrices of the blades, damping matrix of bearings, and gyroscopic matrices of the shaft and rigid disk
g_0	Gap between concentric rotor-blade and casing
J_d, J_p	Diametric and polar mass moments of inertia of the disk
$\boldsymbol{K}_{\text{b1}}$, $\boldsymbol{K}_{\text{b2}}$	Stiffness matrices of the left and right bearings
$k_{\text{b}X}$, $k_{\text{b}Y}$, $k_{\text{b}Z}$	Stiffness of the bearing in X, Y and Z directions
$\boldsymbol{K}_{\text{c}}$	Stiffness matrix of the casing
k_{c}	Equivalent stiffness of the casing
$k_{\text{c}X}$, $k_{\text{c}Y}$	Stiffness of the casing in X and Y directions
$\boldsymbol{K}^{\text{e}}$	Stiffness matrix of the Timoshenko beam element
$\boldsymbol{K}_s$	The stiffness matrix of the shaft
L	Length of the blade
$\boldsymbol{M}_{\text{b}}$, $\boldsymbol{M}_{\text{RB}}$	Mass matrices of the blade and rotor-blade system
$\boldsymbol{M}_{\text{c}}$, $\boldsymbol{M}_{\text{d}}$	Mass matrices of the casing and disk
$\boldsymbol{M}_{\text{c1}}$, $\boldsymbol{M}_{\text{c2}}$, $\boldsymbol{M}_{\text{c3}}$	Coupling terms of mass matrices
$\boldsymbol{M}^{\text{e}}$	mass matrix of the Timoshenko beam element
$\boldsymbol{M}_{\text{s}}$	Mass matrix of the shaft
$M_{\text{rub},X}$, $M_{\text{rub},Y}$, $M_{\text{rub},Z}$	Bending moments at the disk location in θ_X and θ_Y directions and the torque in θ_Z direction
m_{d}	Mass of the disk
N_{b}	Blade number
N_{dof}	Number of DOFs for ith blade
N_{mod}	Number of modal truncation
N_{Ns}	Number of DOFs for the shaft
$\boldsymbol{n}_i$	Unit normal vector to the contact surface for the ith blade
$\boldsymbol{q}_{\text{b}}$, $\boldsymbol{q}_{\text{c}}$, $\boldsymbol{q}_{\text{d}}$, $\boldsymbol{q}_{\text{r}}$, $\boldsymbol{q}_{\text{s}}$, $\boldsymbol{q}_{\text{RB}}$,	Generalized coordinate vectors of the blade, casing, disk, rotor, shaft and rotor-blade system
R_{c}, R_{d}	Radius of the casing and disk
$U_m(t)$, $V_m(t)$, $\psi_m(t)$	Canonical coordinates
$\mathbf{u}_{\text{b}}^i$	Displacement vector of the ith blade in the global coordinate system
$\boldsymbol{u}_{\text{c}}$	Displacement vector of casing
$\boldsymbol{u}_i$	Displacement vector of the ith blade-casing relative motion in the global coordinate system
u, v, w, φ	Longitudinal deformation, lateral deformation, swing deformation and cross-sectional rotation in blade local coordinate system
X_{d}, Y_{d}, Z_{d}	Displacements of the disk in X, Y and Z directions in the global coordinate system

Greek symbols

β	Stagger angle of the blade
δ	The penetration depth
δ_0	Initial penetration depth
δu, δv, $\delta\varphi$	Independence variables of variational operation
$\theta(t)$	The angular displacement of the disk
$\theta_{X\text{d}}$, $\theta_{Y\text{d}}$ and $\theta_{Z\text{d}}$	Swing angle of the disk in X and Y directions and torsional angle of the shaft
$\dot{\theta}$	Angular velocity
κ	Shear correction factor of the blade

μ	Friction coefficient
ξ_1, ξ_2	Modal damping ratios (in this paper, $\xi_1 = \xi_2 = 0.02$)
υ	Poisson's ratio
ρ_b	Material density of the blade
$\phi_{1m}(x), \phi_{2m}(x), \phi_{3m}(x)$	Modal shape functions

1 Introduction

The clearance between the blade and casing is a key parameter of turbine machinery, which influences the gas leakage. For example, a large clearance will lead to a reduction of the compression efficiency in turbine machinery. However, reducing the clearance, which can improve the compression efficiency, will increase the risk of the blade-casing rubbing. Blade vibration caused by blade-tip rubbing and rubbing fault diagnosis are attracting increasing attention [1–4]. Only considering the blade vibration, the rubbing between the blade/bladed-disk and the casing has been investigated, such as Legrand et al. [5,6], Lesaffre et al. [7], Sinha [8,9], Kou and Yuan [10], Yuan and Kou [11], Almeida et al. [12], Batailly et al. [13] and Ma et al. [14,15].

For the blade installed on a flexible rotor system, the rotor whirl has a great influence on the blade-casing rubbing [16]. Many researchers worked on rotor-blade systems and investigated the dynamic characteristics due to the blade-casing rubbing [17–27]. On the basis of a lumped mass model (LMM), Kascak et al. [17] investigated the responses of a rotor-bearing system with smearing or abradable rubbing. Padovan et al. [18] established an LMM of a rotor system and analyzed the single- and multiple-blade rubbings responses considering the influence of unbalance magnitude, blade/rotor stiffness, system damping and rubbing interface friction characteristics. Based on a finite element (FE) model which considers the rubbing between the rigid blade and rigid casing, Lawrence et al. [19] simulated the interactions between the blade and casing. Sinha [20] developed a dynamic model for a bladed rotor system supported by multiple bearings and discussed the transient response of the rotor due to blade-tip rubbing during both the acceleration and deceleration processes. Based on a nonsymmetric bladed rotor system where blades are simulated by pre-twisted thin shallow shells, Sinha [21] analyzed the rubbing load under the blade missing. His simulation results show that the sudden rubbing load can increase by an order of magnitude over the unbalance force. Lesaffre et al. [22] established a flexible bladed rotor model in the rotating frame and observed an unstable phenomenon around the critical speed of the stator even under frictionless sliding. Based on a coupling model of flexible bladed rotor and flexible casing, Parent et al. [23] analyzed the blade-casing rubbing phenomena. Based on Ref. [23], Parent et al. [24] analyzed the effects of 3D contact formulation on both rubbing detection and the system stability due to the blade-casing rubbing. Based on contact dynamics, Ma et al. [25] established a rotor-blade-casing FE model using ANSYS software and analyzed complicated vibration responses caused by the blade-casing rubbing. Petrov [26] proposed a multi-harmonic analysis method to simulate whole-engine vibration due to the blade-casing rubbing, and he also demonstrated the high accuracy and computational efficiency of the proposed methods using a set of test cases and an example of analysis of a realistic gas turbine structure. Thinery et al. [27] studied the dynamic behaviors of a misaligned Kaplan turbine with blade-to-stator contacts. In their model, the rotor is modeled using the FE method with beam elements, while the rigid blades are adopted to deal with the contact between the rotor and casing.

Experimental tests have been used to study the blade-casing rubbing [14,28–33]. By simplifying the blade as a rotating uniform beam and the casing as an arc structure, Ahrens et al. [28] measured contact forces and the contact duration by experiment. Considering the effects of elastic casing, Ma et al. [14] established a test rig of blade-casing rubbing and analyzed the normal rubbing force under different casing materials and rotational speeds. Padova et al. [29,30] established an in-ground spin-pit facility (SPF) whose maximum rotational speed can reach 20000 rev/min and studied the metal-to-metal contact due to sudden penetrations with different penetration depths. Chen et al. [31] carried out rubbing experiments with different rubbing positions by using a rotor experiment rig of aero-engine and analyzed the relation of rubbing feature and rubbing position by the cepstrum. Adopting wavelet analysis to deal with the measured blade-casing rubbing data, Lim and Leong [32] and Abdelrhman et al. [33] detected the changes of rotor dynamics caused by blade-casing rubbing.

From the above literature reviews, it can be observed that most researchers focused on the rubbing between cantilever blades (beam or plate) and casings. The stud-

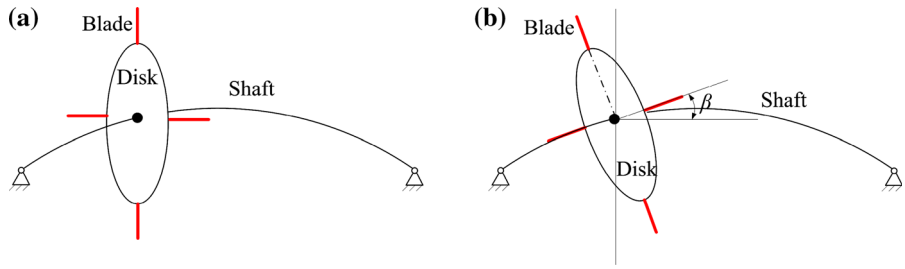

Fig. 1 **a** Neglecting the swing of the disk in Ref. [34], **b** considering the swing of the disk in this study

ies considering both the rotor whirl and the flexibility of the blades are very limited. Based on our previous research works [14,34], the focuses of this paper include:

(1) An improved rotor-blade model is developed. In the improved model, the effects of the swing of the disk are considered (see Fig. 1b); however, they are not considered in Ref. [34] (see Fig. 1a). The proposed model can improve the calculation accuracy, especially under the flexible shaft condition. In addition, the stagger angle of the blade can also be considered in the improved model.

In our previous work [34], the shaft is modeled using lumped-parameter model (lumped mass points); however, it is difficult to accurately determine the masses of these discrete points in this model. In this study, the shaft is modeled using an FE method, which adopts element matrices of mass, stiffness and damping to assemble the whole matrices' of mass, stiffness and damping, and it is convenient to implement for the modeling of the shaft. Furthermore, the mode shapes of rotor-blade systems can be also obtained based on the proposed model, which is also another improvement to the model in Ref. [34].

(2) The rubbings between both the single and four blades and casing are simulated based on a normal rubbing force model presented in our previous work [14]. In Ref. [14], the simulated normal rubbing force is determined using the model in which the blade is presented using a cantilever beam model to represent the blade, and the casing is described using a two DOF model; the simulated normal rubbing force is validated using experimental results. In this study, the rotor whirl is considered, and the bending vibrations of the blades, the lateral and torsional vibrations of the shaft and casing vibration are discussed. In addition, the simulated results are also validated using the measured results in a test rig. Some new coupling vibration phenomena of the rotor-blade-casing system are also evaluated using the experiment results.

The paper is organized as follows. After this introduction, an improved dynamic model of rotor-blade systems is developed using the Hamilton's principle in conjunction with assumed modes method in Sect. 2.1. The proposed model is validated by comparing the natural frequencies obtained from FE method and literature results in Sect. 2.2. A dynamic model of the rotor-blade system with blade-casing rubbing is presented in Sect. 3. In Sect. 4, simulated and measured vibration responses of the system are compared and some typical fault features for single- and four-blade rubbings are summarized. Finally, the conclusions are drawn in Sect. 5.

2 An improved dynamic model of rotor-blade systems

2.1 Dynamic model of rotor-blade systems

Considering the coupling effects of lateral and torsional vibrations of the rotor and longitudinal and bending/flexural vibrations of the blade, a schematic of a rotor-blade system is shown in Fig. 2. The rotor is composed of a shaft and rigid disk. The cantilever Timoshenko beam is used to simulate flexible blade, attached to the rigid disk. In Fig. 2, *OXYZ* is the global coordinate, and $ox^{\mathrm{d}}y^{\mathrm{d}}z^{\mathrm{d}}$ is the disk body coordinate. In addition, $ox^{\mathrm{r}}y^{\mathrm{r}}z^{\mathrm{r}}$ and $ox^{\mathrm{b}}y^{\mathrm{b}}z^{\mathrm{b}}$ represent the rotational coordinate and local coordinate systems of the blade, respectively. Symbols u, v and w represent the deformations in longitudinal, bending/flexural and swing directions of the blade, and φ represents the cross-sectional rotation of the blade in local coordinate system $ox^{\mathrm{b}}y^{\mathrm{b}}z^{\mathrm{b}}$ (see Fig. 3).

The mathematical model of rotor-blade system is simplified according to the following assumptions.

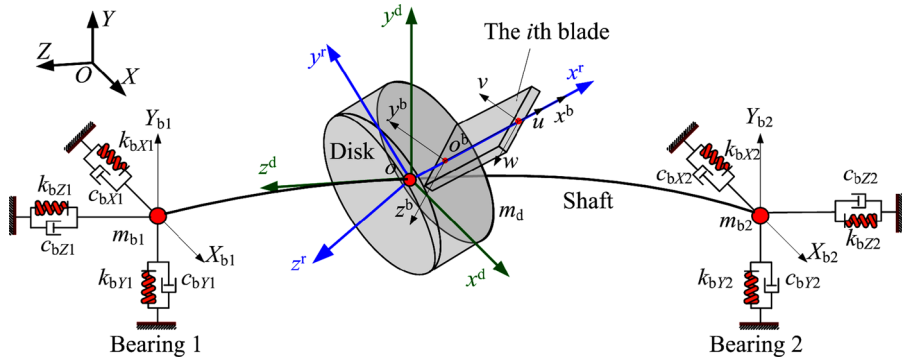

Fig. 2 Schematic of rotor-blade systems

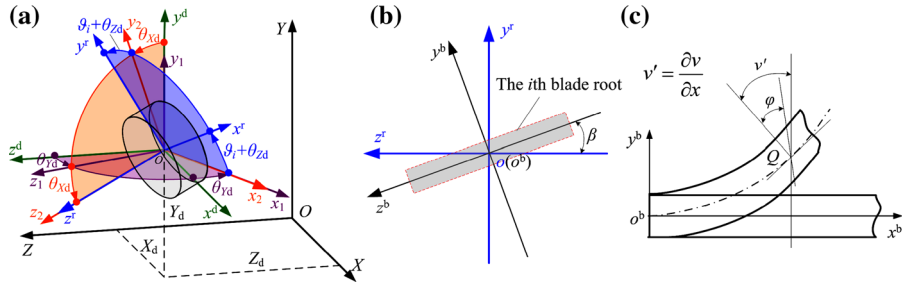

Fig. 3 **a** Coordinate systems of the disk, **b** local coordinate systems of the blade, **c** Timoshenko beam in local coordinate system of the blade

(1) Isotropic material is adopted, and the constitutive relationship satisfies Hooke's law;
(2) The contact problems of the blade, disk and shaft are neglected;
(3) The disk is considered to be rigid, i.e., its flexibility is neglected, and it is described using a lumped mass point;
(4) The shaft is described using FE method;
(5) The blades are represented using uniform cantilever beams;
(6) The bearing is simplified by a linear spring-damping model.

The position vector of any point Q on the blade can be written in the global coordinate system as:

$$\boldsymbol{r}_Q = \begin{bmatrix} X_\mathrm{d} \\ Y_\mathrm{d} \\ Z_\mathrm{d} \end{bmatrix} + \boldsymbol{A}_4\boldsymbol{A}_3\boldsymbol{A}_2\boldsymbol{A}_1 \begin{bmatrix} R_\mathrm{d} + x + u - y\varphi \\ v + y \\ w \end{bmatrix}, \quad (1)$$

where four rotational transformation matrices $\boldsymbol{A}_1$, $\boldsymbol{A}_2$, $\boldsymbol{A}_3$ and $\boldsymbol{A}_4$ are given as follows:

$$\boldsymbol{A}_1 = \begin{bmatrix} 1 & 0 & 0 \\ 0 & \cos\beta & -\sin\beta \\ 0 & \sin\beta & \cos\beta \end{bmatrix}, \quad (2)$$

$$\boldsymbol{A}_2 = \begin{bmatrix} \cos(\vartheta_i + \theta_{Z\mathrm{d}}) & -\sin(\vartheta_i + \theta_{Z\mathrm{d}}) & 0 \\ \sin(\vartheta_i + \theta_{Z\mathrm{d}}) & \cos(\vartheta_i + \theta_{Z\mathrm{d}}) & 0 \\ 0 & 0 & 1 \end{bmatrix}, \quad (3)$$

$$\boldsymbol{A}_3 = \begin{bmatrix} 1 & 0 & 0 \\ 0 & \cos\theta_{X\mathrm{d}} & -\sin\theta_{X\mathrm{d}} \\ 0 & \sin\theta_{X\mathrm{d}} & \cos\theta_{X\mathrm{d}} \end{bmatrix} = \begin{bmatrix} 1 & 0 & 0 \\ 0 & 1 & -\theta_{X\mathrm{d}} \\ 0 & \theta_{X\mathrm{d}} & 1 \end{bmatrix}, \quad (4)$$

$$\boldsymbol{A}_4 = \begin{bmatrix} \cos\theta_{Y\mathrm{d}} & 0 & \sin\theta_{Y\mathrm{d}} \\ 0 & 1 & 0 \\ -\sin\theta_{Y\mathrm{d}} & 0 & \cos\theta_{Y\mathrm{d}} \end{bmatrix} = \begin{bmatrix} 1 & 0 & \theta_{Y\mathrm{d}} \\ 0 & 1 & 0 \\ -\theta_{Y\mathrm{d}} & 0 & 1 \end{bmatrix}. \quad (5)$$

In Eqs. (2)–(5), β is the stagger angle of the blade; $\vartheta_i = \theta(t) + (i-1)\frac{2\pi}{N_\mathrm{b}}$, where $\theta(t)$ is the angular displacement of the disk; $(i-1)\frac{2\pi}{N_\mathrm{b}}$ describes the position of the ith blade in the blade group; θ_{Zd} is a shaft torsional angle at disk hub; and N_b is the number of the blade. It is worth noting that the motion in the swing direction of the blade is neglected, i.e. $w = 0$.

Substituting Eqs. (2)–(5) into Eq. (1) and ignoring high-order terms, $\boldsymbol{r}_Q$ can then be expressed as:

$$\boldsymbol{r}_Q = \begin{bmatrix} \left(\begin{array}{l} X_\mathrm{d} + y\theta_{Y\mathrm{d}} \sin\beta - ((y+v)\cos\beta + (R_\mathrm{d}+x)\,\theta_{Z\mathrm{d}})\sin\vartheta_i \\ +(R_\mathrm{d}+x+u-y\varphi - y\theta_{Z\mathrm{d}}\cos\beta)\cos\vartheta_i \end{array}\right) \\ \left(\begin{array}{l} Y_\mathrm{d} - y\theta_{X\mathrm{d}} \sin\beta + (R_\mathrm{d}+x+u-y\varphi - y\theta_{Z\mathrm{d}}\cos\beta)\sin\vartheta_i \\ +((y+v)\cos\beta + (R_\mathrm{d}+x)\,\theta_{Z\mathrm{d}})\cos\vartheta_i \end{array}\right) \\ \left(\begin{array}{l} Z_\mathrm{d} + (y+v)\sin\beta + (y\theta_{Y\mathrm{d}}\cos\beta + (R_\mathrm{d}+x)\,\theta_{X\mathrm{d}})\sin\vartheta_i \\ +(y\theta_{X\mathrm{d}}\cos\beta - (R_\mathrm{d}+x)\,\theta_{Y\mathrm{d}})\sin\vartheta_i \end{array}\right) \end{bmatrix}. \tag{6}$$

The expressions of total kinetic energy T_total and total potential energy V_total for the SDB system are as follows:

$$\begin{aligned} T_\mathrm{total} &= \sum_{i=1}^{N_\mathrm{b}} T_\mathrm{blade} + T_\mathrm{shaft} + T_\mathrm{disk}, \\ V_\mathrm{total} &= \sum_{i=1}^{N_\mathrm{b}} V_\mathrm{blade} + V_\mathrm{shaft} + V_\mathrm{bearing} \end{aligned} \tag{7}$$

where T_blade, T_shaft and T_disk are the kinetic energy of the blade, shaft and disk, and V_blade, V_shaft and V_disk are the potential energy of the blade, shaft and disk, respectively. More details about these energy expressions can refer to [34] and the specific matrices and vectors formulas can be found in "Appendix".

The equations of motion of the rotor system and blade system are assembled together to form the global matrices of the rotor-blade system. The schematic of the matrix assembling is shown in Fig. 4 where N_dof is the number of DOFs for the ith blade, and $N_{N\mathrm{s}}$ is the number of DOFs for the rotor.

Equations of motion of the rotor-blade system can then be written as follows:

$$\begin{aligned} &\boldsymbol{M}_\mathrm{RB}\ddot{\boldsymbol{q}}_\mathrm{RB} + (\boldsymbol{C}_\mathrm{RB} + \boldsymbol{G}_\mathrm{RB})\dot{\boldsymbol{q}}_\mathrm{RB} + \boldsymbol{K}_\mathrm{RB}\boldsymbol{q}_\mathrm{RB} \\ &\quad = \boldsymbol{F}_\mathrm{nonlinear} + \boldsymbol{F}_\mathrm{rub}, \end{aligned} \tag{8}$$

where $\boldsymbol{M}_\mathrm{RB}$ is the mass matrix of the system; $\boldsymbol{C}_\mathrm{RB}$ is the viscous damping matrix of the system, which is simulated by the Rayleigh damping; $\boldsymbol{G}_\mathrm{RB}$ is the other damping matrix of the system except for viscous damping matrix, which includes the Coriolis force matrices of the blades, damping matrix of bearings, and gyroscopic matrices of the shaft and rigid disk; $\boldsymbol{K}_\mathrm{RB}$ is the stiffness matrix of the system; $\boldsymbol{q}_\mathrm{RB}$ is the generalized displacement vector; and $\boldsymbol{F}_\mathrm{nonlinear}$ and $\boldsymbol{F}_\mathrm{rub}$ are the nonlinear coupling force vector and rubbing force vector, respectively.

In the equation, generalized displacement vector of rotor-blade systems $\boldsymbol{q}_\mathrm{RB}$ can be expressed as:

$$\boldsymbol{q}_\mathrm{RB} = \begin{bmatrix} \boldsymbol{q}_\mathrm{b} & \boldsymbol{q}_\mathrm{s} \end{bmatrix}^\mathrm{T}, \tag{9}$$

where $\boldsymbol{q}_\mathrm{b}$ and $\boldsymbol{q}_\mathrm{s}$ are the displacement vectors of the blade and shaft, respectively.

The nonlinear force vector $\boldsymbol{F}_\mathrm{nonlinear}$ can be expressed as:

$$\boldsymbol{F}_\mathrm{nonlinear} = [\boldsymbol{F}_\mathrm{nonlinear,\,b} \quad \boldsymbol{F}_\mathrm{nonlinear,\,s}]^\mathrm{T}, \tag{10}$$

where $\boldsymbol{F}_\mathrm{nonlinear,b}$ is the nonlinear force vector of the blade (see "Appendix 5"). $\boldsymbol{F}_\mathrm{nonlinear,s}$ is the nonlinear force vector of the shaft and its expression can be given as follows:

$$\begin{aligned} \boldsymbol{F}_\mathrm{nonlinear,s} = [0 \ \cdots\ & f_{\mathrm{nonlinear},X} \ f_{\mathrm{nonlinear},Y} \ f_{\mathrm{nonlinear},Z} \\ & M_{\mathrm{nonlinear},X} \ M_{\mathrm{nonlinear},Y} \\ & M_{\mathrm{nonlinear},Z} \ \cdots\ 0]^\mathrm{T}, \end{aligned} \tag{11}$$

where $f_{\mathrm{nonlinear},X}$, $f_{\mathrm{nonlinear},Y}$, $f_{\mathrm{nonlinear},Z}$, $M_{\mathrm{nonlinear},X}$, $M_{\mathrm{nonlinear},Y}$ and $M_{\mathrm{nonlinear},Z}$ are nonlinear forces and moments applied at the disk position (see "Appendix 5").

Rayleigh damping matrix $\boldsymbol{C}_\mathrm{RB}$ can be expressed as:

$$\boldsymbol{C}_\mathrm{RB} = \zeta \boldsymbol{M}_\mathrm{RB} + \eta \boldsymbol{K}_\mathrm{RB}, \tag{12}$$

$$\begin{cases} \zeta = \frac{4\pi f_{\mathrm{n}1} f_{\mathrm{n}2}(\xi_1 f_{\mathrm{n}2} - \xi_2 f_{\mathrm{n}1})}{(f_{\mathrm{n}2}^2 - f_{\mathrm{n}1}^2)} \\ \eta = \frac{\xi_2 f_{\mathrm{n}2} - \xi_1 f_{\mathrm{n}1}}{\pi(f_{\mathrm{n}2}^2 - f_{\mathrm{n}1}^2)} \end{cases}, \tag{13}$$

where $f_{\mathrm{n}1}$ and $f_{\mathrm{n}2}$ represent the first and second natural frequency (Hz) of the rotor-blade system, respectively, and ξ_1 and ξ_2 (in this paper, $\xi_1 = \xi_2 = 0.02$) are the corresponding modal damping ratios.

2.2 Model verification based on natural characteristics

In this section, a flexible rotor-blade model is used to verify the proposed model, and the detailed rotor-blade physical dimensions are shown in Fig. 5 and Table 1. The detailed elements used to describe the shaft, disk, blades and bearings can be found in Ref. [34]. The natural frequencies are calculated using both methods [34], including an FE modeling method and an analytical method.

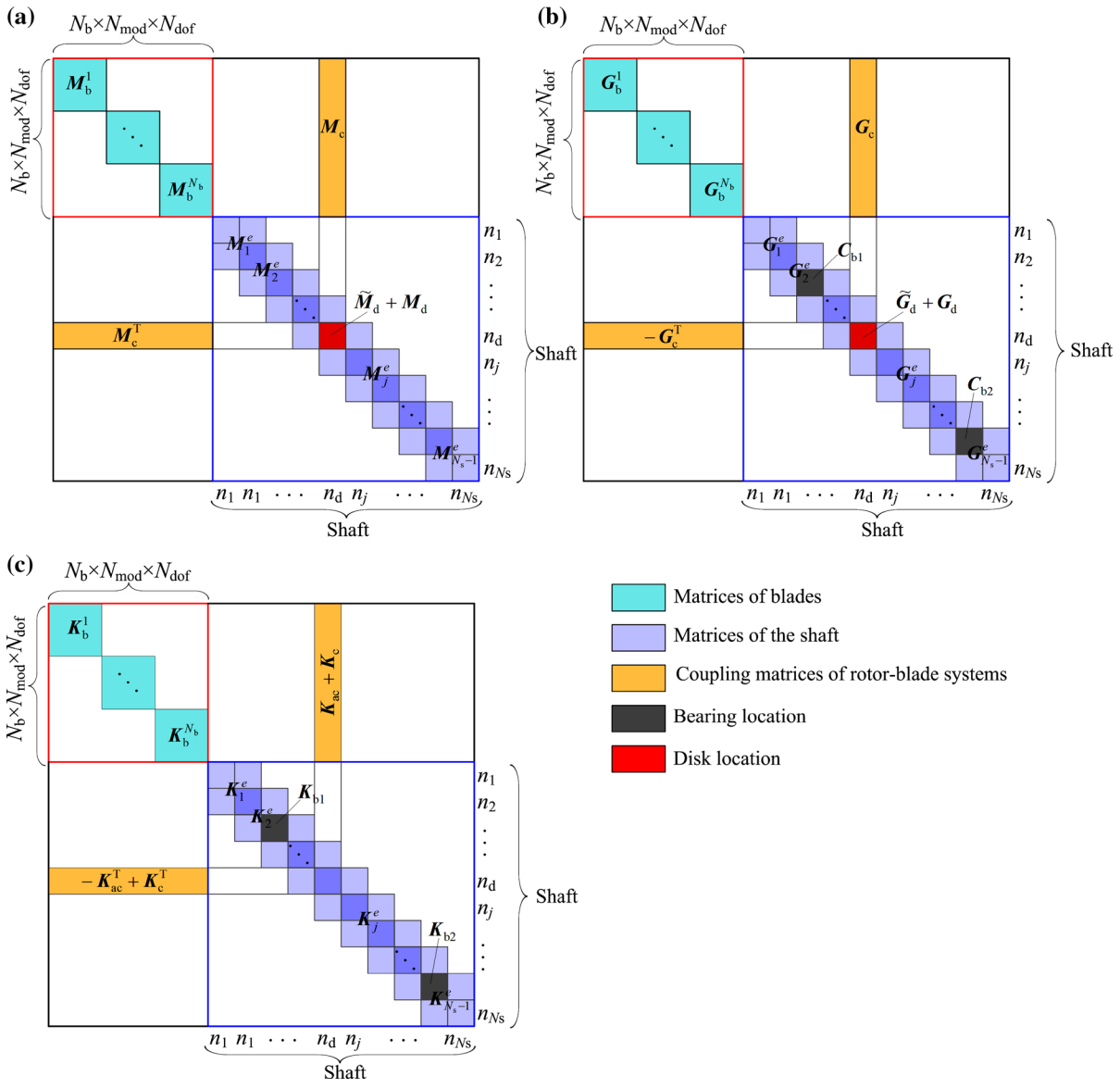

Fig. 4 Schematic diagram of assembled matrices for rotor-blade systems: **a** mass matrix $\boldsymbol{M}_{\mathrm{RB}}$, **b** damping matrix $\boldsymbol{G}_{\mathrm{RB}}$, **c** stiffness matrix $\boldsymbol{K}_{\mathrm{RB}}$

The results are shown in Table 2. The natural frequencies determined using FE and analytical methods in [34] are given in the second and third columns. The fifth and sixth columns show the percentage differences between the analytical model in Ref. [34] and the proposed model relative to the results of the FE model, respectively. The results in Table 2 show that the proposed model has a higher accuracy than that of the analytical method in Ref. [34], especially, for the vibration modes related to the disk swing. For example, the percentage differences of natural frequencies related to the disk swing (f_{n4} and f_{n5}) reduce from 3.9340 % for the analytic model in [34] to 0.1042 % for the proposed model. Moreover, the mode shapes obtained from the proposed model also show a good agreement with those obtained from the FE model, as shown in Fig. 6.

Besides the comparison with the FE model, the model is also validated by comparing the natural frequencies obtained from the proposed model with those from Yang's method in Ref. [35], as shown in Table 3.

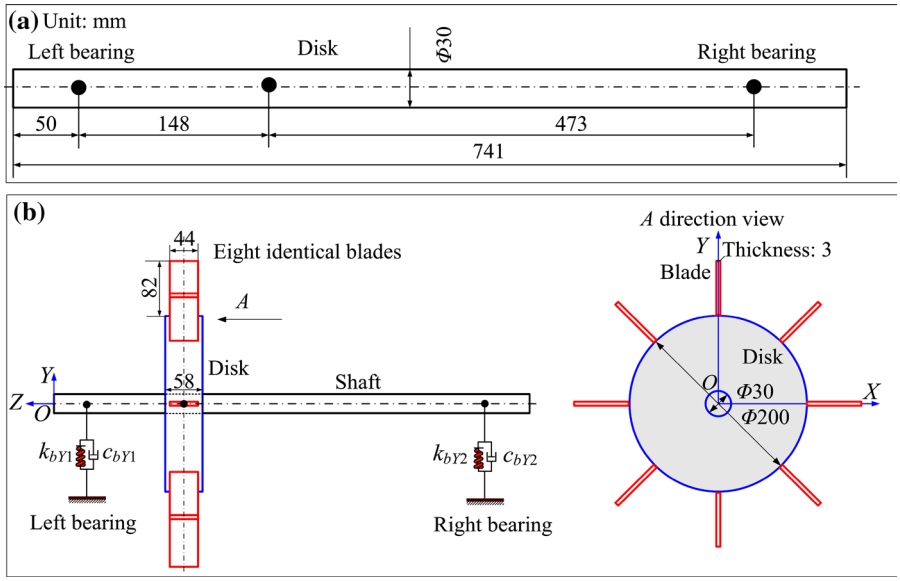

Fig. 5 Physical dimensions of a rotor-blade system: **a** physical dimensions of the shaft, **b** physical dimensions of the disk and blade

Table 1 Model parameters of the rotor-blade system

Parts	Geometric parameters	Material parameters
Shaft	See Fig. 5	$\rho = 7800\ \text{kg/m}^3$ $E = 200\ \text{GPa}$ $\upsilon = 0.3$
Bearing	$k_{bX1} = k_{bX2} = k_{bY1} = k_{bY2} = 1.5 \times 10^7\ \text{N/m}$, $c_{bX1} = c_{bX2} = c_{bY1} = c_{bY2} = 1 \times 10^3\ \text{N s/m}$	
Blade	See Fig. 5	
Disk	$m_d = 13.89\ \text{kg}$, $J_p = 0.071\ \text{kg m}^2$, $J_d = 0.0394\ \text{kg m}^2$	

The results obtained from the proposed method are in good agreement with those obtained from Yang's method, and the maximum percentage difference of the natural frequency is 4.7919 %. The trends of some natural frequencies (see Table 3) are the same as that in Ref. [35]. Some natural frequencies do not change because the coupling effect between the disk and blade is not considered for the proposed model.

3 A dynamic model of rotor-blade systems with blade-casing rubbing

Rubbing between the blade-tip and casing can happen due to the rotor whirl and blade elongation. A schematic of blade-casing rubbing forces is shown in Fig. 7 where F_{n}^i and F_{t}^i are the normal and tangential rubbing forces applied on the ith rubbing blade, respectively. For the shaft, F_{n}^i can be translated and equivalent to a force F_{nr}^i, and F_{t}^i can be equivalent to a force F_{tr}^i and a torque M_{tr}^i, as shown in the left figure of Fig. 7. For the rubbing blade, the direction of F_{n}^i along the blade pointing toward the disk center, and the tangential rubbing force F_{t}^i in the local coordinate system of the blade can be decomposed into two forces F_{tz}^i and F_{ty}^i, as shown in the right figure of Fig. 7.

Considering the influence of the casing vibration on the blade-tip rubbing and simplifying the casing as an LMP with two DOFs, the equations of motion of the rotor-blade-casing system can be written as follows:

$$\begin{cases} \boldsymbol{M}_{\text{RB}}\ddot{\boldsymbol{q}}_{\text{RB}} + (\boldsymbol{C}_{\text{RB}} + \boldsymbol{G}_{\text{RB}})\dot{\boldsymbol{q}}_{\text{RB}} + \boldsymbol{K}_{\text{RB}}\boldsymbol{q}_{\text{RB}} = \boldsymbol{F}_{\text{RB}} \\ \boldsymbol{M}_{\text{c}}\ddot{\boldsymbol{q}}_{\text{c}} + \boldsymbol{D}_{\text{c}}\dot{\boldsymbol{q}}_{\text{c}} + \boldsymbol{K}_{\text{c}}\boldsymbol{q}_{\text{c}} = \boldsymbol{F}_{\text{c}} \end{cases}, \tag{14}$$

where $\boldsymbol{M}_{\text{c}}$, $\boldsymbol{D}_{\text{c}}$ and $\boldsymbol{K}_{\text{c}}$ are mass, damping and stiffness matrices of the casing, respectively; $\boldsymbol{q}_{\text{c}}$ and $\boldsymbol{F}_{\text{c}}$ are the generalized coordinate vector and rubbing force vector of the casing, respectively. In this equation, the external force $\boldsymbol{F}_{\text{RB}} = \boldsymbol{F}_{\text{nonlinear}} + \boldsymbol{F}_{\text{rub}}$, where $\boldsymbol{F}_{\text{nonlinear}}$ (see

Table 2 Natural frequencies comparison of the rotor-blade system

Natural frequencies	FE model [34]	Analytical model [34]	Proposed model	Percentage differences between FE model and analytical model [34] (%)	Percentage differences between FE model and proposed model (%)
f_{n1}	57.87	57.88	57.88	0.0173	0.0173
f_{n2}	61.09	61.25	61.08	0.2616	0.0164
f_{n3}	61.09	61.25	61.08	0.2616	0.0164
f_{n4}	258.91	**269.30**	**259.18**	3.9340	0.1042
f_{n5}	258.91	**269.30**	**259.18**	3.9340	0.1042
f_{n6}	364.57	364.72	364.72	0.0411	0.0411
f_{n7}	364.57	364.72	364.72	0.0411	0.0411
f_{n8}	364.57	364.72	364.72	0.0411	0.0411
f_{n9}	364.57	364.72	364.72	0.0411	0.0411
f_{n10}	364.57	364.72	364.72	0.0411	0.0411
f_{n11}	367.26	367.50	367.41	0.0653	0.0408
f_{n12}	367.26	367.50	367.41	0.0653	0.0408
f_{n13}	390.12	390.25	390.25	0.0333	0.0333
f_{n14}	443.30	**453.95**	**444.78**	2.3739	0.3333
f_{n15}	443.30	**453.95**	**444.78**	2.3739	0.3333

$f_{ni}\,(i = 1, 2, \ldots, 15)$ denotes the ith natural frequency. Percentage difference equals the absolute value of the change in value, divided by the average of the two numbers, all multiplied by 100. Percentage difference $= \frac{|V_1 - V_2|}{(V_1+V_2)/2} \times 100$ (%) where V_2 denotes a reference value and V_1 is a target value

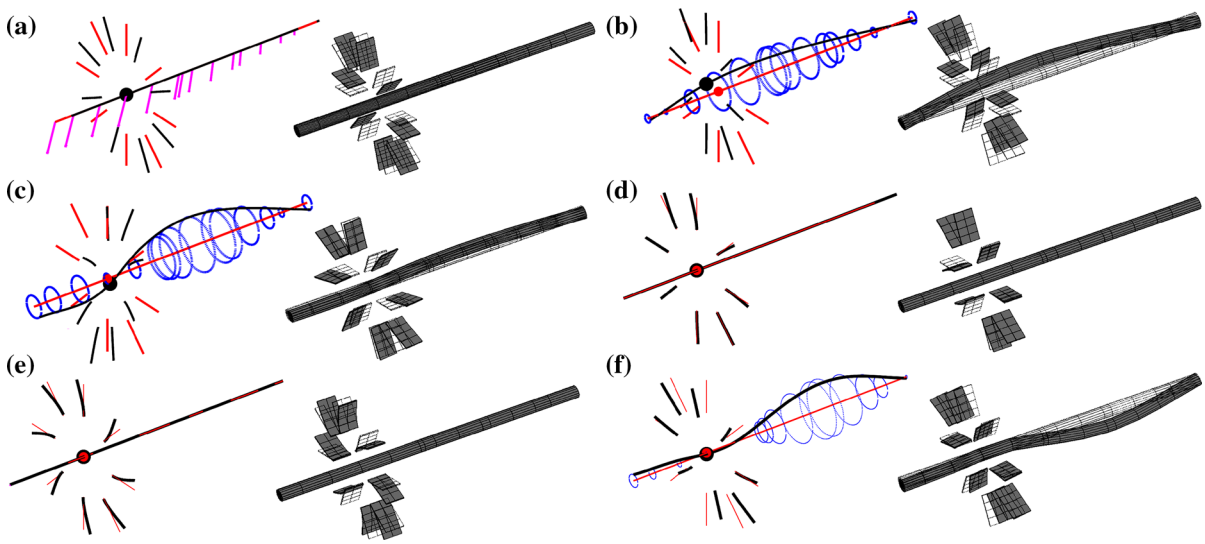

Fig. 6 Comparison of mode shapes: **a** f_{n1}, **b** f_{n2}, **c** f_{n4}, **d** f_{n7}, **e** f_{n13}, **f** f_{n14}

"Appendix 5") and $\boldsymbol{F}_{\text{rub}}$ are the nonlinear force vector and rubbing force vector of the rotor-blade system, respectively.

The expression of $\boldsymbol{F}_{\text{rub}}$ is

$$\boldsymbol{F}_{\text{rub}} = \left[\underbrace{\boldsymbol{F}_{\text{rub, b}}}_{\text{Blade}} \quad \underbrace{0 \quad \boldsymbol{F}_{\text{rub, d}} \quad 0}_{\text{Rotor}} \right]^{\text{T}}. \tag{15}$$

Table 3 Natural frequencies comparison of a rotor-blade system considering stagger angles

Stagger angles	Orders	Yang's model [35] (Hz)	Proposed model (Hz)	Percentage differences between Yang's model [35] and proposed model (%)
$\beta = \pi/6$	1	80.77	80.7632	0.0084
	2	81.423	81.542	0.1460
	3	81.438	81.542	0.1276
	4	81.496	81.542	0.0564
	5	81.538	81.542	0.0049
	6	81.538	81.542	0.0049
	7	201.921	200.0141	0.9489
	8	498.517	513.186	2.8999
	9	499.185	513.186	2.7660
	10	507.924	513.186	1.0306
	11	510.99	513.186	0.4288
	12	510.99	513.186	0.4288
	13	514.986	517.5091	0.4887
$\beta = \pi/4$	1	81.011	81.0165	0.0068
	2	81.309	81.542	0.2862
	3	81.339	81.542	0.2493
	4	81.455	81.542	0.1068
	5	81.538	81.542	0.0049
	6	81.538	81.542	0.0049
	7	198.269	196.3806	0.9570
	8	492.757	513.186	4.0617
	9	493.538	513.186	3.9034
	10	505.373	513.186	1.5341
	11	510.99	513.186	0.4288
	12	510.99	513.186	0.4288
	13	513.067	515.9525	0.5608
$\beta = \pi/3$	1	81.197	81.2760	0.0972
	2	81.241	81.542	0.3698
	3	81.257	81.542	0.3501
	4	81.414	81.542	0.1571
	5	81.538	81.542	0.0049
	6	81.538	81.542	0.0049
	7	194.759	192.8798	0.9696
	8	489.17	513.186	4.7919
	9	489.954	513.186	4.6319
	10	503.201	513.186	1.9648
	11	510.99	513.186	0.4288
	12	510.99	513.186	0.4288
	13	511.33	514.5159	0.6211

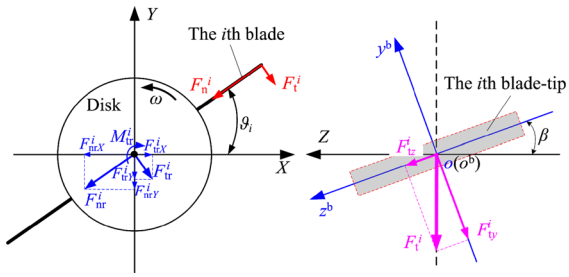

Fig. 7 Schematic of blade-casing rubbing forces

The rubbing force vector $\boldsymbol{F}_{\mathrm{rub,b}}$ of the blades can be written as $\boldsymbol{F}_{\mathrm{rub,b}} = \left[\cdots \ \boldsymbol{F}^i_{\mathrm{rub,\,b}} \ \cdots\right]$ where $\boldsymbol{F}^i_{\mathrm{rub,\,b}}$ denotes the rubbing force vector of the ith rubbing blade and it can be expressed as

$$\boldsymbol{F}^i_{\mathrm{rub,b}} = \begin{bmatrix} -F^i_{\mathrm{n}}\ \phi_{1m}|_{x=L} \\ -F^i_{\mathrm{t}}\cos\beta\phi_{2m}\big|_{x=L} \\ 0 \end{bmatrix}^{\mathrm{T}}. \tag{16}$$

The rubbing force vector applied on the disk $\boldsymbol{F}_{\mathrm{rub,d}}$ is

$$\boldsymbol{F}_{\mathrm{rub,d}} = \sum_{i=1}^{N_{\mathrm{b}}} \begin{bmatrix} F^i_{\mathrm{t}}\sin\vartheta_i - F^i_{\mathrm{n}}\cos\vartheta_i \\ -F^i_{\mathrm{t}}\cos\vartheta_i - F^i_{\mathrm{n}}\sin\vartheta_i \\ 0 \\ 0 \\ 0 \\ -(R_{\mathrm{d}}+L)\,F^i_{\mathrm{t}} \end{bmatrix}^{\mathrm{T}}. \tag{17}$$

The expressions of $\boldsymbol{M}_{\mathrm{c}}$, $\boldsymbol{D}_{\mathrm{c}}$, $\boldsymbol{K}_{\mathrm{c}}$, $\boldsymbol{q}_{\mathrm{c}}$ and $\boldsymbol{F}_{\mathrm{c}}$ are given as follows:

$$\boldsymbol{M}_{\mathrm{c}} = \begin{bmatrix} m_{\mathrm{c}} & 0 \\ 0 & m_{\mathrm{c}} \end{bmatrix}, \quad \boldsymbol{K}_{\mathrm{c}} = \begin{bmatrix} k_{\mathrm{c}X} & 0 \\ 0 & k_{\mathrm{c}Y} \end{bmatrix},$$

$$\boldsymbol{D}_{\mathrm{c}} = \begin{bmatrix} c_{\mathrm{c}X} & 0 \\ 0 & c_{\mathrm{c}Y} \end{bmatrix} + \zeta\boldsymbol{M}_c + \eta\boldsymbol{K}_c, \tag{18}$$

$$\boldsymbol{q}_{\mathrm{c}} = \begin{bmatrix} X_{\mathrm{c}} & Y_{\mathrm{c}} \end{bmatrix}^{\mathrm{T}},$$

$$\boldsymbol{F}_{\mathrm{c}} = \sum_{i=1}^{N_{\mathrm{b}}} \begin{bmatrix} -F^i_{\mathrm{t}}\sin\vartheta_i + F^i_{\mathrm{n}}\cos\vartheta_i \\ F^i_{\mathrm{t}}\cos\vartheta_i + F^i_{\mathrm{n}}\sin\vartheta_i \end{bmatrix}, \tag{19}$$

where m_{c} is the casing mass; $c_{\mathrm{c}X}$ and $c_{\mathrm{c}Y}$ are damping of the casing; $k_{\mathrm{c}X}$ and $k_{\mathrm{c}Y}$ are stiffness of the casing; X_{c} and Y_{c} are displacements of the casing. The subscripts X and Y denote X and Y directions, respectively.

Normal rubbing force F_{n} can be expressed as [14]:

$$F_{\mathrm{n}} = -\left(L\Gamma_1 k_{\mathrm{c}}\frac{-5\left(\alpha\Gamma_1 - 2\frac{\delta}{L}\right) + \sqrt{5}\alpha\sqrt{5\Gamma_1\left(\Gamma_1 + \frac{4}{\alpha}\frac{\delta}{L}\right) + 12\mu^2\frac{\delta}{L}}}{20\Gamma_1 - \frac{10}{\alpha}\frac{\delta}{L} + 6\alpha\mu^2}\right), \tag{20}$$

where δ is the penetration depth; k_{c} is the equivalent stiffness of the casing, here, $k_{\mathrm{c}} = k_{\mathrm{c}X}$; μ is the friction coefficient; $\Gamma_1 = \frac{\Gamma_0}{k_{\mathrm{c}}}$; $\Gamma_0 = E_{\mathrm{b}}I_{\mathrm{b}}\frac{3}{L^3} + \rho_{\mathrm{b}}A_{\mathrm{b}}\dot{\theta}^2\left(\frac{81}{280}L + \frac{3}{8}R_{\mathrm{d}}\right)$; $\alpha = \frac{R_{\mathrm{d}}+L}{L}$. Minus sign denotes the direction of normal rubbing force is from blade-tip to the center of rotor.

The penetration depth δ, which is related to the radial elongation of the blade, is caused by centrifugal loads and relative geometric position between the blade-tip and casing (see Fig. 8). In the published literature, the effects of the casing distortion are usually considered in the calculation of the blade-casing relative positions [13,26]. It is worth noting that in our study, the effects of the casing distortion are not considered because only a small arc-shaped casing (see Fig. 8) is used to simulate the local blade-casing rubbing in the test rig. The disk and the casing are concentric in the original position (see Fig. 8a), and g_0 is the gap between the concentric bladed disk and casing, $g_0 = R_{\mathrm{c}} - (R_{\mathrm{d}} + L) \geq 0$, where R_{c} is the radius of the casing. However, due to assembling misalignment, the clearance between rotor and stator can be asymmetrical. Hence, the blade tip may penetrate the casing due to the rotor whirl motion and centrifugal force (see Fig. 8b).

The expression of penetration depth between the ith blade and casing is obtained as [26]:

$$\delta^i(t) = \boldsymbol{u}_i^{\mathrm{T}}\boldsymbol{n}_i - g_0, \tag{21}$$

where $\boldsymbol{n}_{\mathrm{i}}$ is unit normal vector to the contact surface.

$$\boldsymbol{n}_i = \begin{bmatrix}\cos\vartheta_i & \sin\vartheta_i\end{bmatrix}^{\mathrm{T}},$$

and $\boldsymbol{u}_{\mathrm{i}}$ is a vector of the ith blade-casing relative motion in the global coordinate,

$$\boldsymbol{u}_i = \boldsymbol{u}^i_{\mathrm{b}} - \boldsymbol{u}_{\mathrm{c}} - \boldsymbol{e}_{\mathrm{c}},$$

where $\boldsymbol{e}_{\mathrm{c}}$ is the eccentricity vector related to the misalignment of the rotor and casing centers; $\boldsymbol{e}_{\mathrm{c}} = \begin{bmatrix} e_X & e_Y \end{bmatrix}^{\mathrm{T}}$; $\boldsymbol{u}^i_{\mathrm{b}}$ and $\boldsymbol{u}_{\mathrm{c}}$ are the displacement vectors of the ith blade-tip and casing in the global coordinate, respectively.

$$\boldsymbol{u}^i_{\mathrm{b}} = \begin{bmatrix} X_{\mathrm{d}} \\ Y_{\mathrm{d}} \\ Z_d \end{bmatrix} + \boldsymbol{A}_4\boldsymbol{A}_3\boldsymbol{A}_2\boldsymbol{A}_1 \begin{bmatrix} u_i \\ v_i \\ 0 \end{bmatrix},$$

$$\boldsymbol{u}_{\mathrm{c}} = \boldsymbol{q}_{\mathrm{c}} = \begin{bmatrix} X_{\mathrm{c}} & Y_{\mathrm{c}} \end{bmatrix}^{\mathrm{T}},$$

$$\vartheta_i = \theta(t) + (i-1)\frac{2\pi}{N_{\mathrm{b}}}. \tag{22}$$

Tangential force F_{t} is generated from the friction between the blade-tip and casing, of which the direction is opposite to slip direction on the contact surface.

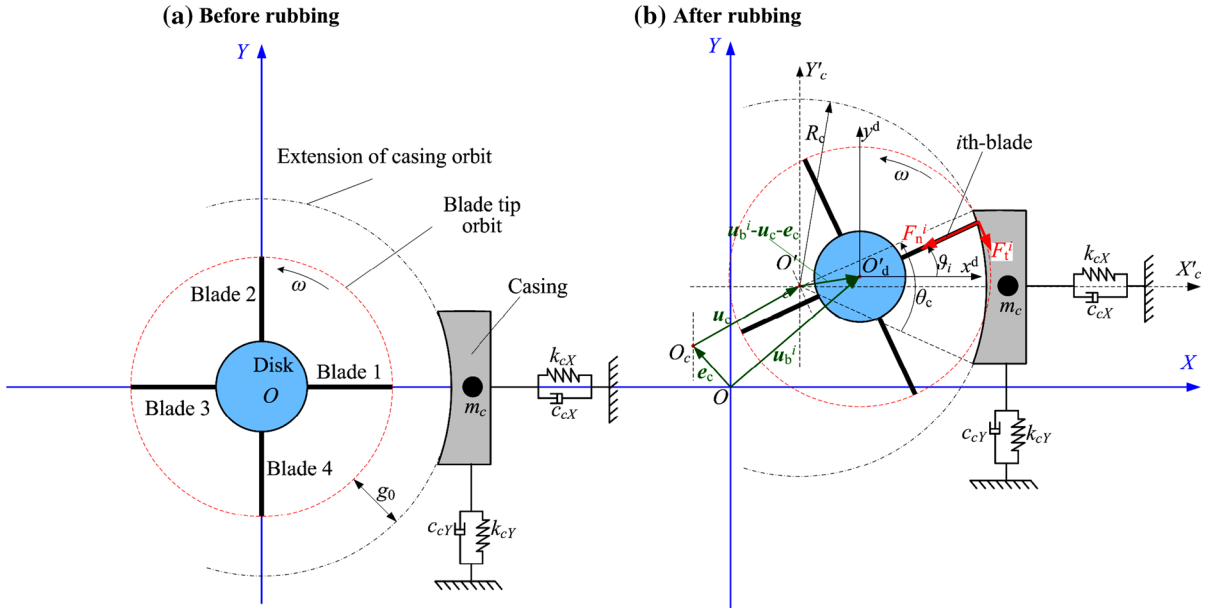

Fig. 8 Schematic of blade-casing rubbing

Hence, tangential force can be written as:

$$F_{\mathrm{t}} = \mu F_{\mathrm{n}}. \tag{23}$$

Because of the effects of the blade-tip rubbing, the equations of motion of the rotor-blade-casing system are nonlinear. In this study, Newmark integral method is adopted to calculate the system vibration response. The detailed simulation flowchart is shown in Fig. 9.

4 Numerical studies and experimental verification

The physical dimensions of a rotor-blade system in the test rig are the same as those in Ref. [34]. For the rotor-blade system, the bearing stiffness in horizontal and vertical directions are set as $k_{bX1} = k_{bY1} = k_{bX2} = k_{bY2} = 1.5 \times 10^7$ N/m. The bearing stiffness in axial direction are $k_{bZ1} = k_{bZ2} = 4 \times 10^6$ N/m. The bearing damping in three directions are $c_{bX1} = c_{bY1} = c_{bX2} = c_{bY2} = c_{bZ1} = c_{bZ2} = 1000$ Ns/m. The stagger angle of the blade is $\beta = 0°$. It is worth noting that the torsional DOF of the right-most node (node 11) is restrained while that of the left-most node (node 1) is free, which is another revision to the system in Ref. [34]. This is because that the right end of the shaft is connected with the driving motor by a coupling in this study. Other parameters are the same as those in Ref. [34]. The simulated and measured natural frequencies of the rotor-blade system are shown in Table 4. This results show that the proposed model has a higher accuracy than the model in Ref. [34]. Percentage differences of the natural frequencies $f_{\mathrm{n}5}$ and $f_{\mathrm{n}6}$ decrease from 4.3973 % in Ref. [34] to 3.1661 % in this study (see Table 4).

In order to evaluate the rubbing-induced casing vibration, the natural frequencies of the casing system without and with blade-casing contact are also measured using the same test rig [34]. The measured natural frequencies are listed in Table 5.

Assuming that both the directions of the rotor whirl of rotation are counterclockwise, and the whirl velocity and the rotational speed are the same, in this section, two kinds of rubbing forms: single- and four-blade rubbings will be simulated. In addition, the experimental results are also used to validate the simulated results. The simulation parameters are set as follows:

Eccentricity between the geometrical center of the rotor-blade system and its mass center is 1 mm. The casing mass is $m_c = 5$ kg and casing stiffness in horizontal and vertical directions are $k_{cX} = 3 \times 10^6$ N/m and $k_{cY} = 7 \times 10^7$ N/m, i.e., the natural frequencies of the casing in X and Y directions are 123.3 and 595.5 Hz, respectively. The casing damping in horizontal and vertical directions are $c_{cX} = c_{cY} = 2000$ Ns/m. The radius of the casing is $R_{\mathrm{c}} = 224$ mm, the vector of the eccentricity is $\boldsymbol{e}_{\mathrm{c}} = [e_X \quad e_Y]^{\mathrm{T}}$, $e_X = g_0 + \delta_0$ ($g_0 = 2$ mm), $e_Y = 0$ where δ_0 is the initial penetration depth.

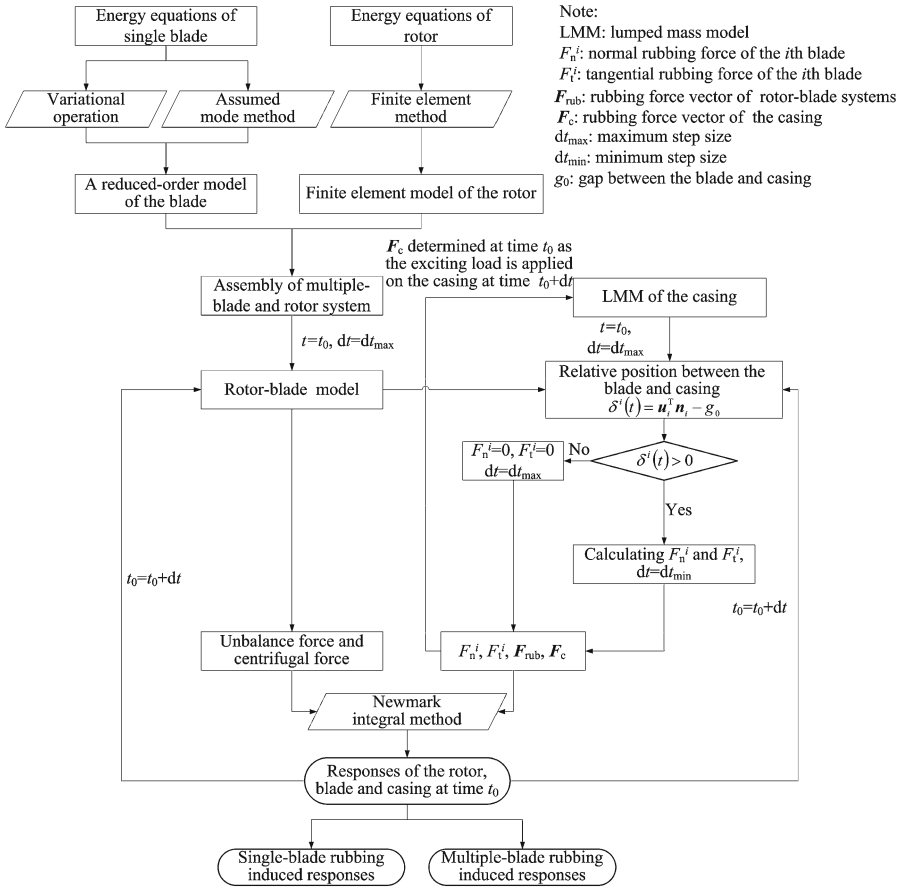

Fig. 9 Flowchart of blade-casing rubbing simulation

Table 4 Natural frequencies of the rotor-blade system at zero rotational speed

Orders	Proposed model (Hz)	Experiment [34]	Descriptions of mode shapes	Percentage differences between proposed model and experimental results (%)
1 (f_{n1})	78.6	–	Axial vibration	–
2 (f_{n2})	132.9	129.3	Conical mode in lateral direction	2.7460
3 (f_{n3})	132.9	129.3	Conical mode orthogonal with f_{n2}	2.7460
4 (f_{n4})	156.6	–	Torsional vibration	–
5 (f_{n5})	266.3	258.0	Swing of the disk	3.1661
6 (f_{n6})	266.3	258.0	Swing of the disk orthogonal with f_{n5}	3.1661
7 (f_{n7})	364.7	361.3	Blade-blade coupling mode	0.9366
8 (f_{n8})	365.4	364.7	Coupling mode between the rotor lateral and blade bending vibrations	0.1918
9 (f_{n9})	365.4	368.0	Coupling mode orthogonal with f_{n8}	0.7090
10 (f_{n10})	371.3	372.0	Coupling mode between the rotor torsional and blade bending vibrations	0.1883

"–" denotes no value

Table 5 Natural frequencies of the casing system without and with blade-casing contact

Orders	1 (f_{nc1})	2 (f_{nc2})	3 (f_{nc3})	4 (f_{nc4})	5 (f_{nc5})	6 (f_{nc6})
Casing system without blade-casing contact (Hz)	124.1	197.8	585.3	834.1	1020.0	1161.0
Orders	1 (f_{ncr1})	2 (f_{ncr2})	3 (f_{ncr3})	4 (f_{ncr4})	5 (f_{ncr5})	
Casing system with blade-casing contact (Hz)	173.4	581.9	980.9	1205.0	1443.0	

Table 6 Parameters for simulation and experiment under five cases

Rubbing forms	Cases	Rotational speeds (rev/min)	Initial penetration depths δ_0(μm)
No rubbing	1	986.4 (16.44 Hz)	0
Single-blade rubbing	2	986.4 (16.44 Hz)	50
	3	1478.4 (24.64 Hz)	50
Four-blade rubbing	4	976.8 (16.28 Hz)	50
	5	1491 (24.85 Hz)	50

The friction coefficient between the blade and casing is $\mu = 0.2$.

Five cases are selected to compare the simulated results with experimental results: healthy condition (case 1), single-blade rubbing condition (cases 2 and 3), and four-blade rubbing condition (cases 4 and 5), as are listed in Table 6. It should be noted that one slightly longer blade is artificially assembled under the single-blade rubbing condition, and four blades with the same dimension is assembled under the four-blade rubbing condition.

4.1 No rubbing condition

The comparison of simulated and measured vibration responses are shown in Fig. 10. The simulated lateral vibration of the rotor in X direction only contains the rotational frequency component (f_r). However, the measured result shows multiple frequency components (nf_r) and a frequency component between $2f_r$ and $3f_r$, which may be excited by the rotor misalignment and bearing nonlinearity. There are also some errors about the vibration amplitude due to the effects of the assumed bearing stiffness, unbalance, and system damping.

4.2 Single-blade rubbing condition

Assuming that the rubbing between only single blade (blade 1) and casing appears, a comparison of simulated and experimental results under case 2 is shown in Figs. 11 and 12, respectively. For the simulated results, rotor vibration (node 9) in lateral (X) and torsional (θ_Z) directions, casing vibration in X direction, blade bending vibrations in local coordinate of the blades, and normal rubbing forces, are used to analyze the fault features. For the experimental results, only the rotor lateral vibration, casing vibration, and normal and tangential rubbing forces are obtained due to some limitations in experimental equipments. Based on the results in Figs. 11 and 12, some dynamic phenomena can be observed as follows:

(1) Simulated results show that amplitude amplification phenomena occur when the multiple frequency components coincide with the natural frequencies of the system. The amplification phenomena can be observed at $8f_r$ near the conical natural frequencies (f_{n2} and f_{n3} in Table 4), $8f_r$ near the casing natural frequency, $10f_r$ near the torsional natural frequency (f_{n4} in Table 4), and $22f_r$ near the bending natural frequencies of the blades (f_{n7}, f_{n8}, f_{n9} and f_{n10} in Table 4), as shown in Fig. 11. The enlargement degrees for the torsional vibration of the rotor, casing vibration and blade bending vibration are more significant than that of the lateral vibration of the rotor.

(2) The measured results also show the similar amplification phenomena when the multiple frequency components coincide with the conical natural fre-

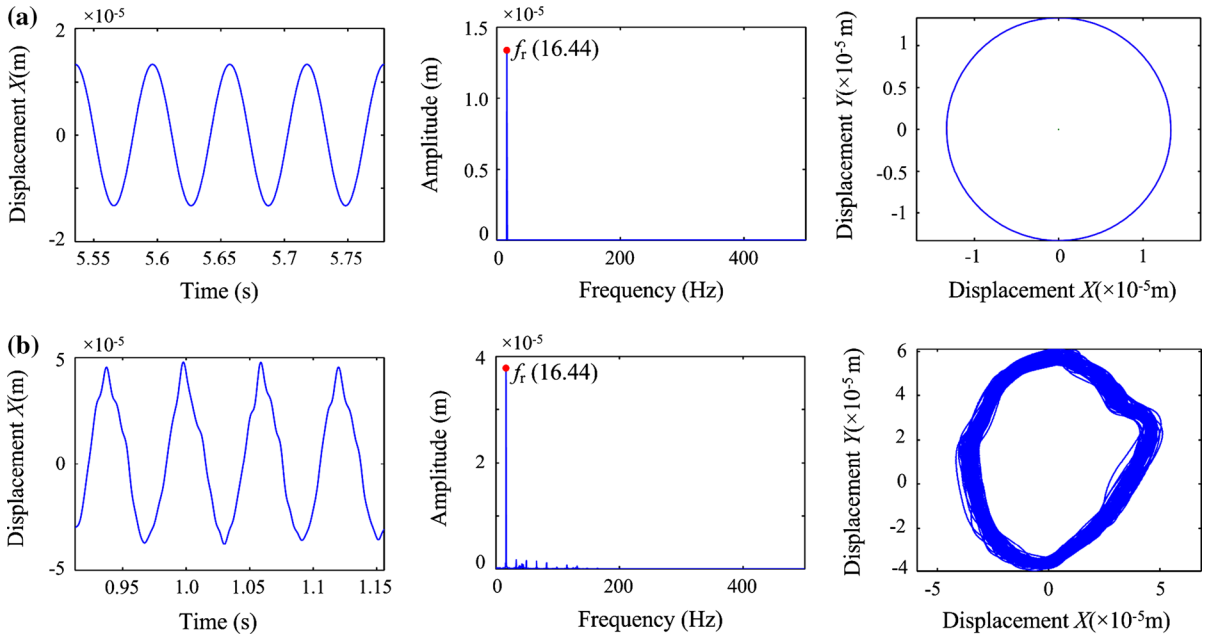

Fig. 10 Vibration responses of the rotor-blade system without rubbing: **a** simulated results, **b** experimental results. *Note* The figures from left to right are time-domain waveform, amplitude spectrum and rotor orbit, respectively

quencies (see Fig. 12b). The casing vibration shows that the amplification phenomena appear at $7f_r$ which is related to the casing natural frequency ($f_{nc1} = 124.1$ Hz, see Table 5). In addition, other higher multiple frequency components at $58f_r$ and $70f_r$ which coincide with the casing natural frequencies f_{ncr3} (or f_{nc5}) and f_{nc6}, respectively, also show large amplitudes. Based on the ratio of the maximum tangential rubbing force and corresponding normal rubbing force in a rotational period, the dynamic friction coefficient is about 0.166, as shown in Fig. 12f, g.

(3) The measured rubbing forces and casing vibration have a significant difference from the simulated results. Main reasons for these errors are that (1) the casing is overly simplified. Actually, the casing is a complicated assembly, and the simulation can only consider the first natural frequency; (2) the assumed system damping, bearing stiffness, amount of unbalance have some differences with those in real system; and (3) accurately controlling the penetration depth is difficult due to the micro-feeding errors of ballscrew driving, which may also lead to some errors between the simulated and measured rubbing forces.

Simulated and measured responses of the system under case 3 are shown in Figs. 13 and 14. Compared with those under case 2, some new vibration features are summarized as follows:

(1) Under the higher rotational speeds, the rotor lateral vibration increase due to the increase of the rubbing level which can be justified by the increased normal rubbing force. The dynamic friction coefficient slightly decreases from 0.166 under case 2 (986.4 rev/min) to 0.158 under case 3 (1478.4 rev/min).

(2) Some frequencies, at which amplification phenomena are observed, may lightly change due to the effects of rubbing nonlinearity on the system natural frequencies. For example, $48f_r$ under case 3 are slightly larger than $70f_r$ under case 2.

4.3 Four-blade rubbing condition

Simulated and measured results under case 4 are shown in Figs. 15 and 16, which show the following dynamic phenomena.

(1) For the simulated results, amplitude amplification phenomena can also be observed, for example, $8f_r$ related to the conical natural frequencies

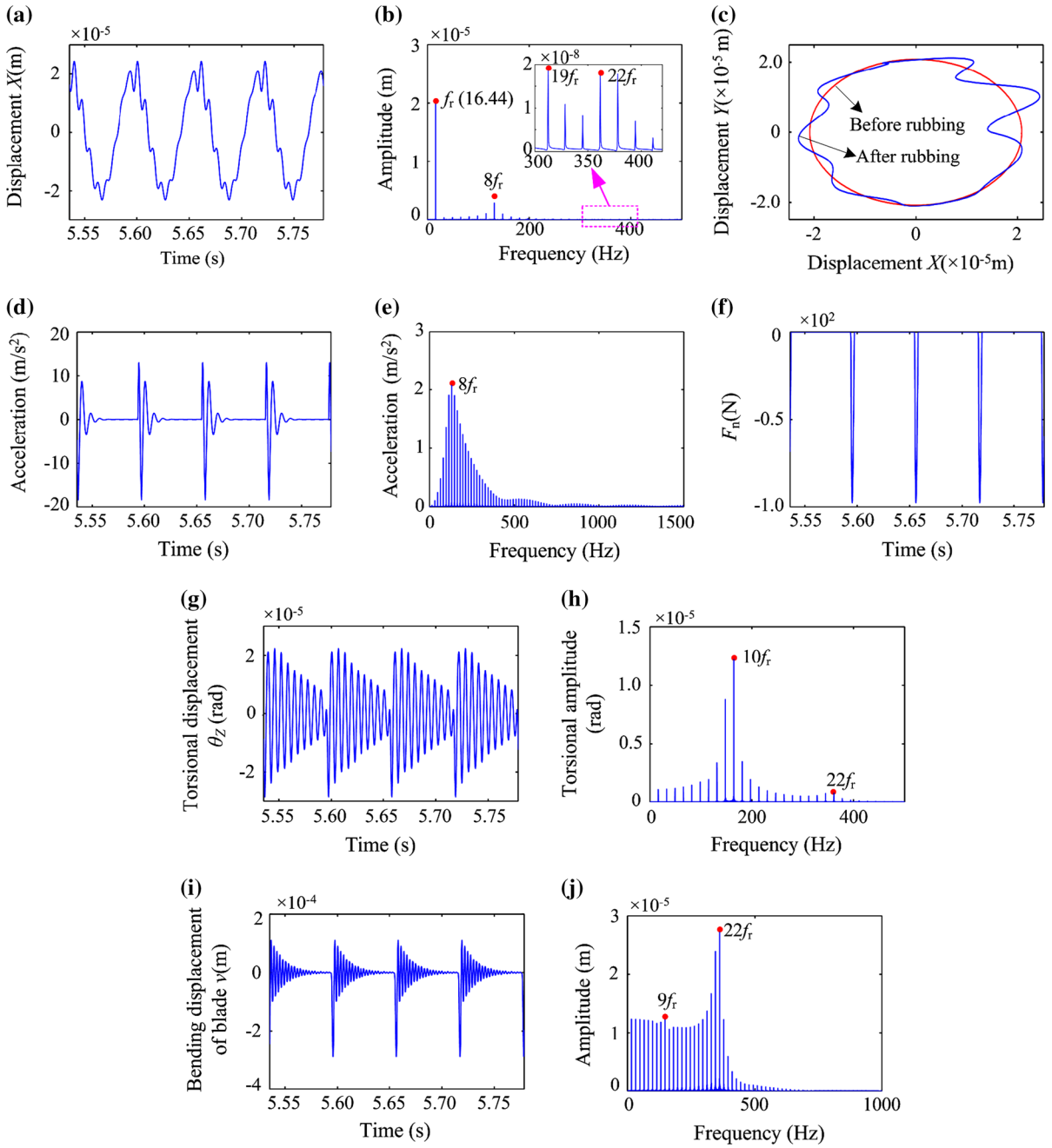

Fig. 11 Simulated results with four-blade rubbing (case 2): **a** rotor displacement waveform in X direction, **b** amplitude spectrum of the rotor in X direction, **c** rotor orbit, **d** acceleration waveform of casing in X direction, **e** amplitude spectrum of casing acceleration in X direction, **f** normal rubbing force, **g** torsional displacement waveform of the rotor, **h** torsional amplitude spectrum of the rotor, **i** bending displacement of the rubbing blade (blade 1), **j** amplitude spectrum of bending displacement of the rubbing blade (blade 1)

(see Fig. 15b) and casing natural frequency (see Fig. 15e), $9\,f_r$ related to the torsional natural frequency (see Fig. 15h), and $22\,f_r$ related to the bending natural frequencies of the blades (see Fig. 15j). For the four-blade rubbing, bigger amplitudes can also be observed at the blade passing frequency

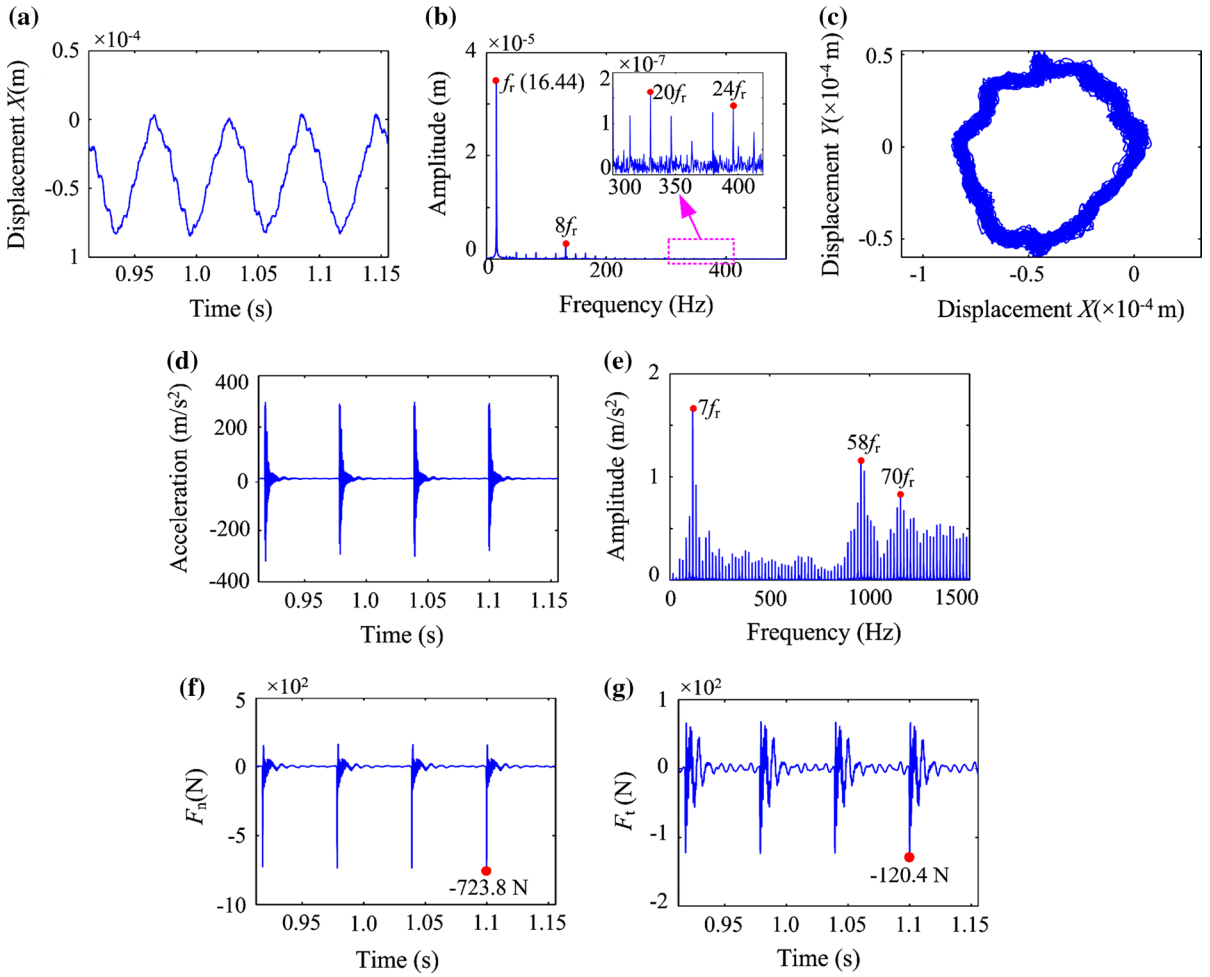

Fig. 12 Experimental results under case 2: **a** time-domain waveform of the rotor in X direction, **b** amplitude spectrum of the rotor, **c** rotor orbit, **d** time-domain waveform of the casing in X direction, **e** amplitude spectrum of the casing, **f** normal rubbing force, **g** tangential rubbing force

(BPF, $4f_r$) and its multiple frequencies, such as BPF, 2BPF, 3BPF, 4BPF, 5BPF and 6BPF, i.e., $4f_r$, $8f_r$, $12f_r$, $16f_r$, $20f_r$ and $24f_r$ (see Fig. 15b, e, h).

(2) For the measured results, both the lateral vibration of the rotor and casing vibration show the amplitude amplification phenomena which agree well with the simulated results. The similar experimental results were also reported in Ref. [32].

The measured normal and tangential rubbing forces under the four-blade and single-blade rubbing conditions have some differences. There are some reasons for these: (1) In order to generate rubbing for the four blades, some blades were grinded, and the lengths of these blades were reduced. (2) The natural frequencies of the mechanical structure, e.g., the triaxial force sensor, are excited by the contact forces, which lead to an amplification and a phase distortion of the force signals [28]. For the four-blade rubbing, the effect of the transient vibration of the force sensor on the measured results increases due to the reducing rubbing period. (3) The control of the penetration depths can also lead to some errors. These reasons also cause large errors in the dynamic friction coefficients for the four blades. So the dynamic friction coefficients are not suggested to be measured under four-blade rubbing conditions, and dynamic friction coefficients under this condition will not be compared in the following analysis.

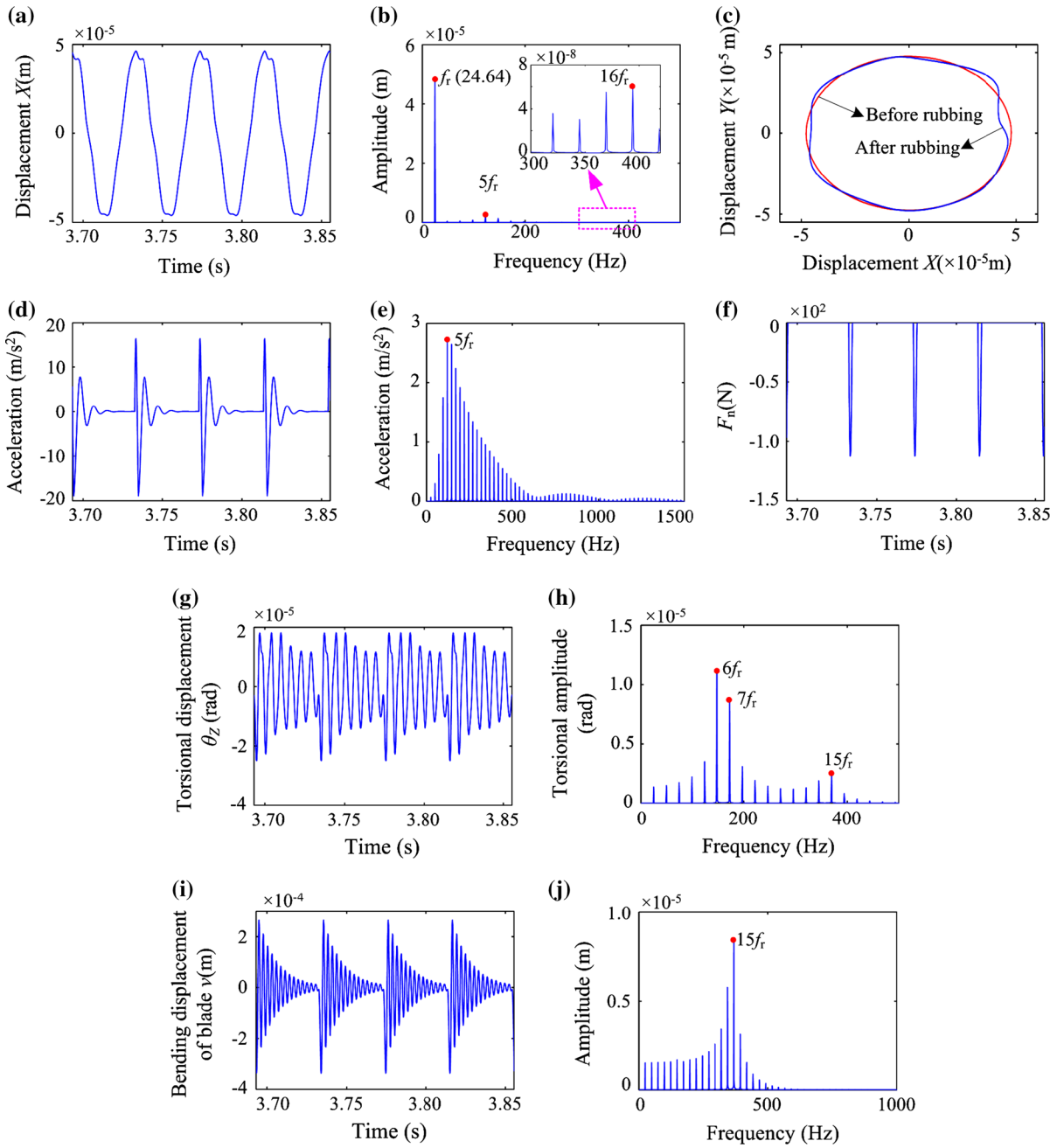

Fig. 13 Simulated results with four-blade rubbing (case 3): **a** rotor displacement waveform in *X* direction, **b** amplitude spectrum of the rotor in *X* direction, **c** rotor orbit, **d** acceleration waveform of casing in *X* direction, **e** amplitude spectrum of casing acceleration, **f** normal rubbing force, **g** torsional displacement waveform of the rotor, **h** torsional amplitude spectrum of the rotor, **i** bending displacement of the rubbing blade (blade 1), **j** amplitude spectrum of bending displacement of the rubbing blade (blade 1)

(3) Simulated and measured spectra show that the amplitude amplification phenomena often appear at the BPF and its multiple frequencies. These features are especially obvious for the amplitude spectrum of the measured casing vibration, which indicates that the rubbing-induced casing vibration can

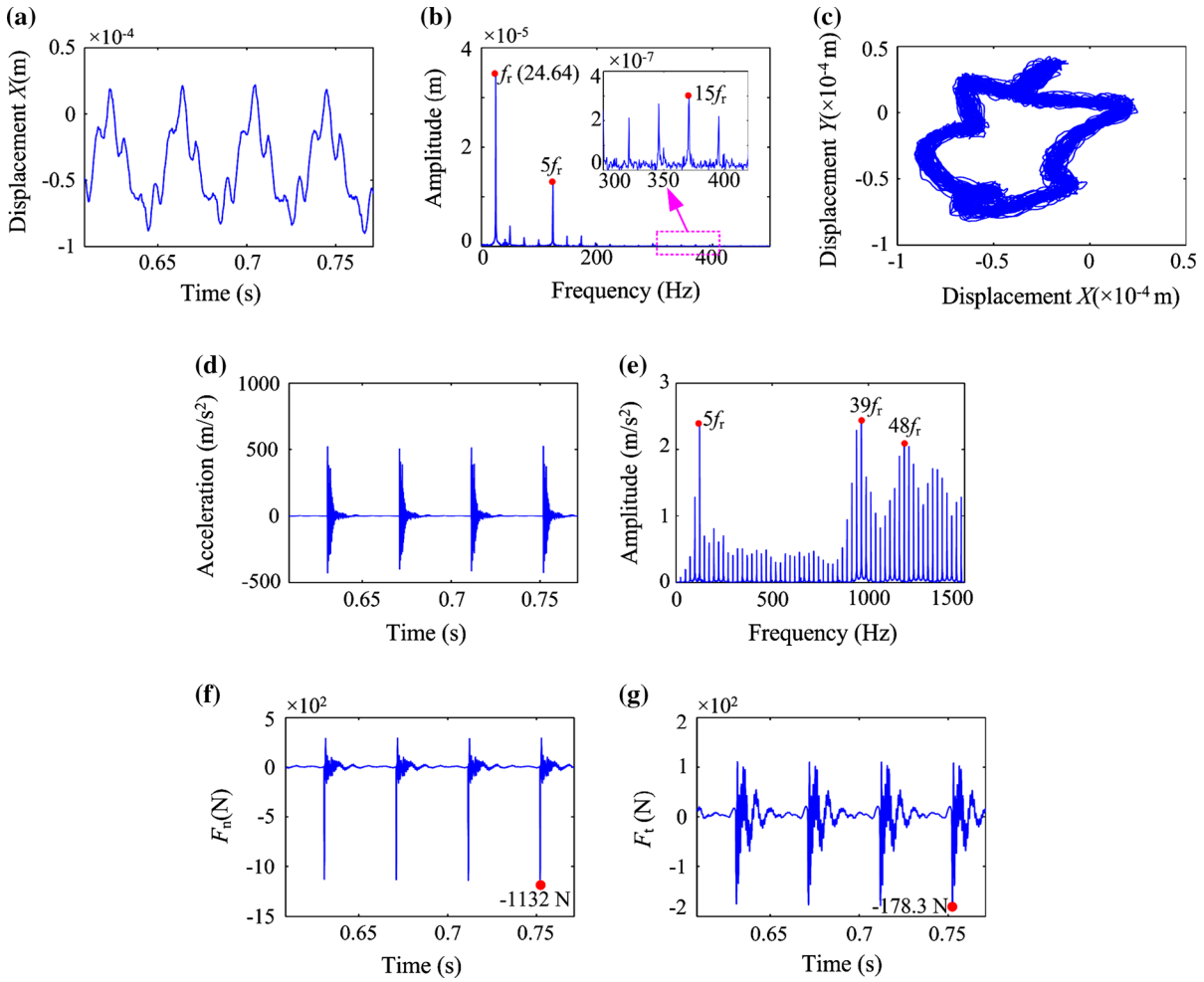

Fig. 14 Experimental results under case 3: **a** time-domain waveform of the rotor in X direction, **b** amplitude spectrum of the rotor, **c** rotor orbit, **d** time-domain waveform of the casing in X direction, **e** amplitude spectrum of the casing, **f** normal rubbing force, **g** tangential rubbing force

appear at the high-order natural frequencies (see Fig. 16e).

(4) Simulated and measured normal rubbing forces show that the rubbing level of blade 1 is most severe, and those of blades 2 and 3 are moderate, and that of blade 4 is the least severe. A detailed explanation can be found in Fig. 17, which shows that the penetration depth is maximal for blade 1, followed by those for blade 2 and blade 4, and minimal for blade 3. In addition, it is also possible that the rubbing between the blade 3 and casing may not appear due to the effects of rotor whirl under small penetration depths.

The simulated results under case 5 are shown in Fig. 18, the similar amplitude amplification phenomena and frequency distributed features related to BPF can be observed. In addition, the rubbing between the blade 3 and casing does not appear. This also verifies the above analysis (see Fig. 17). By increasing the penetration from 50μm to 80μm, the simulated results are shown in Fig. 19, which shows that the four-blade rubbing appears under relatively large penetration depths. Fig. 20 shows the measured results of four-blade rubbing under case 5. The collision levels under case 5 are slightly different from the above analysis under case 4. The penetration depths cannot accurately agree with

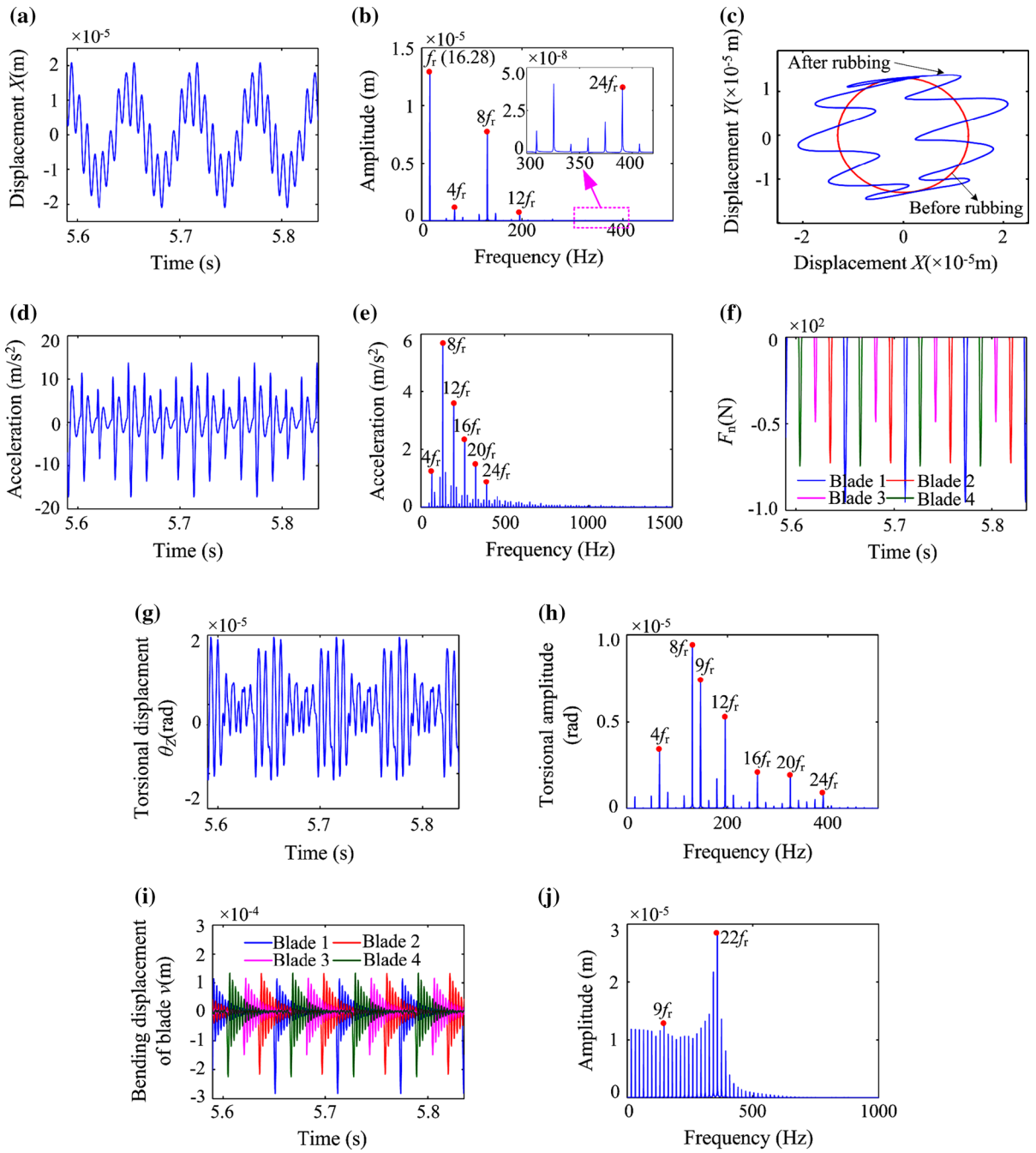

Fig. 15 Simulated results with four-blade rubbing (case 4): **a** rotor displacement waveform in X direction, **b** amplitude spectrum of the rotor in X direction, **c** rotor orbit, **d** acceleration waveform of casing in X direction, **e** amplitude spectrum of casing acceleration, **f** normal rubbing force, **g** torsional displacement waveform of the rotor, **h** torsional amplitude spectrum of the rotor, **i** bending displacements of the blades, **j** amplitude spectrum of bending displacements of the blade 1

the simulated conditions. This may lead to the difference between the simulated and measured results. In addition, the blade-casing abrasions can also lead to the change of the clearance between the blade and casing, which also affects the measured results to some extent.

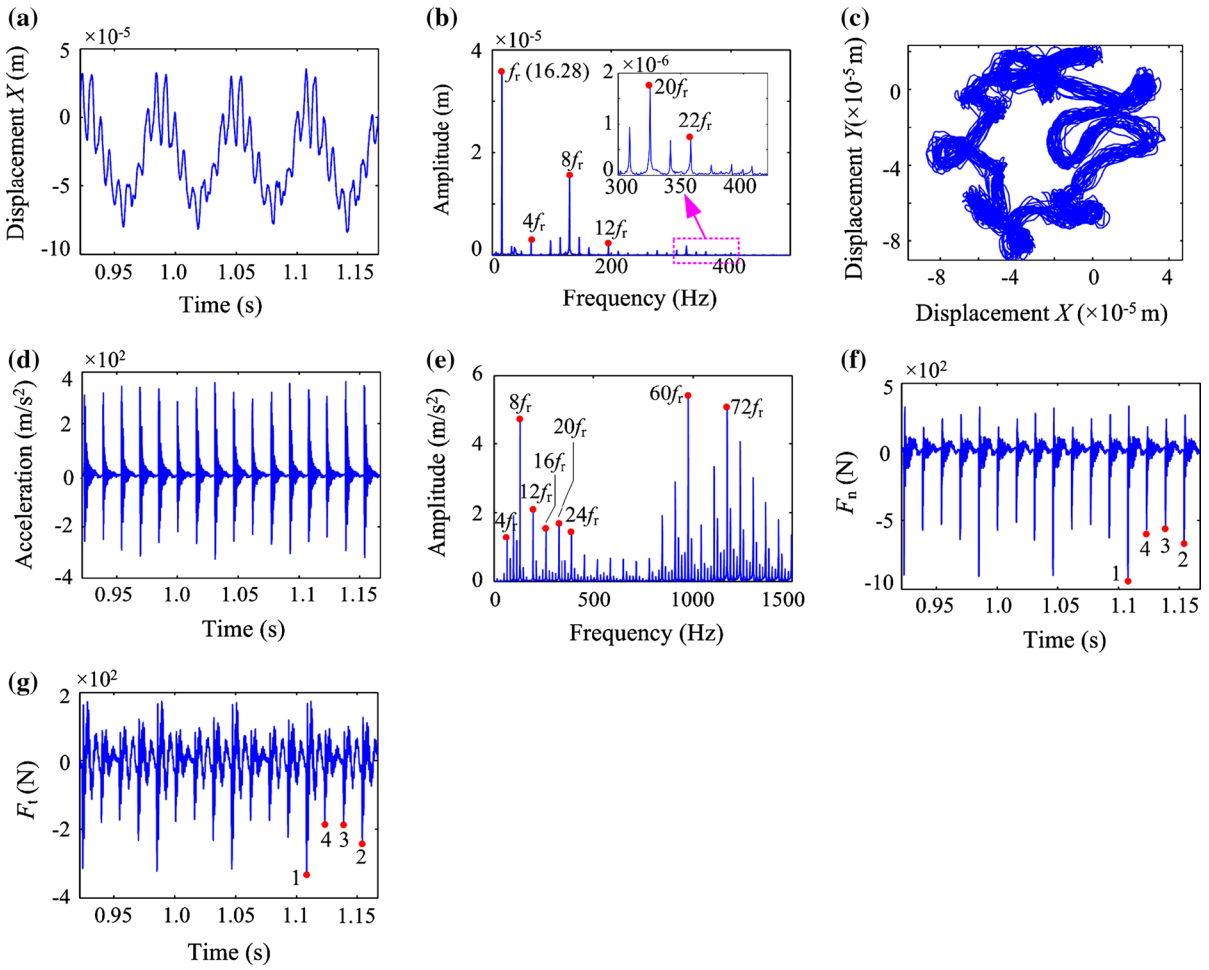

Fig. 16 Experimental results under case 4: **a** time-domain waveform of the rotor in *X* direction, **b** amplitude spectrum of the rotor, **c** rotor orbit, **d** time-domain waveform of the casing in *X*direction, **e** amplitude spectrum of the casing, **f** normal rubbing force, **g** tangential rubbing force. *Note* Numbers *1*, *4*, *3* and *2* denote the rubbing time for blades *1*, *4*, *3* and *2*

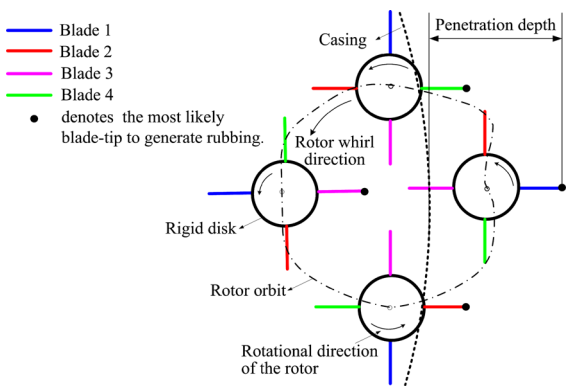

Fig. 17 A schematic of blade-casing rubbing explanation

4.4 Summary of rubbing fault features

Typical fault features for single- and four-blade rubbings are listed in Table 7. For the single-blade rubbing, simulated results show that the amplitude amplification phenomena can be observed when the multiple frequency components of rotational frequency (f_r) coincide with the conical natural frequencies, torsional natural frequency of the rotor-blade system, casing natural frequency and bending natural frequencies of the blades. For the four-blade rubbing, simulated results show that BPF and its multiple frequency components (nBPF, $n = 1, 2, 3, \ldots$) with larger amplitudes can be viewed as a distinguished feature besides the amplitude amplification phenomena.

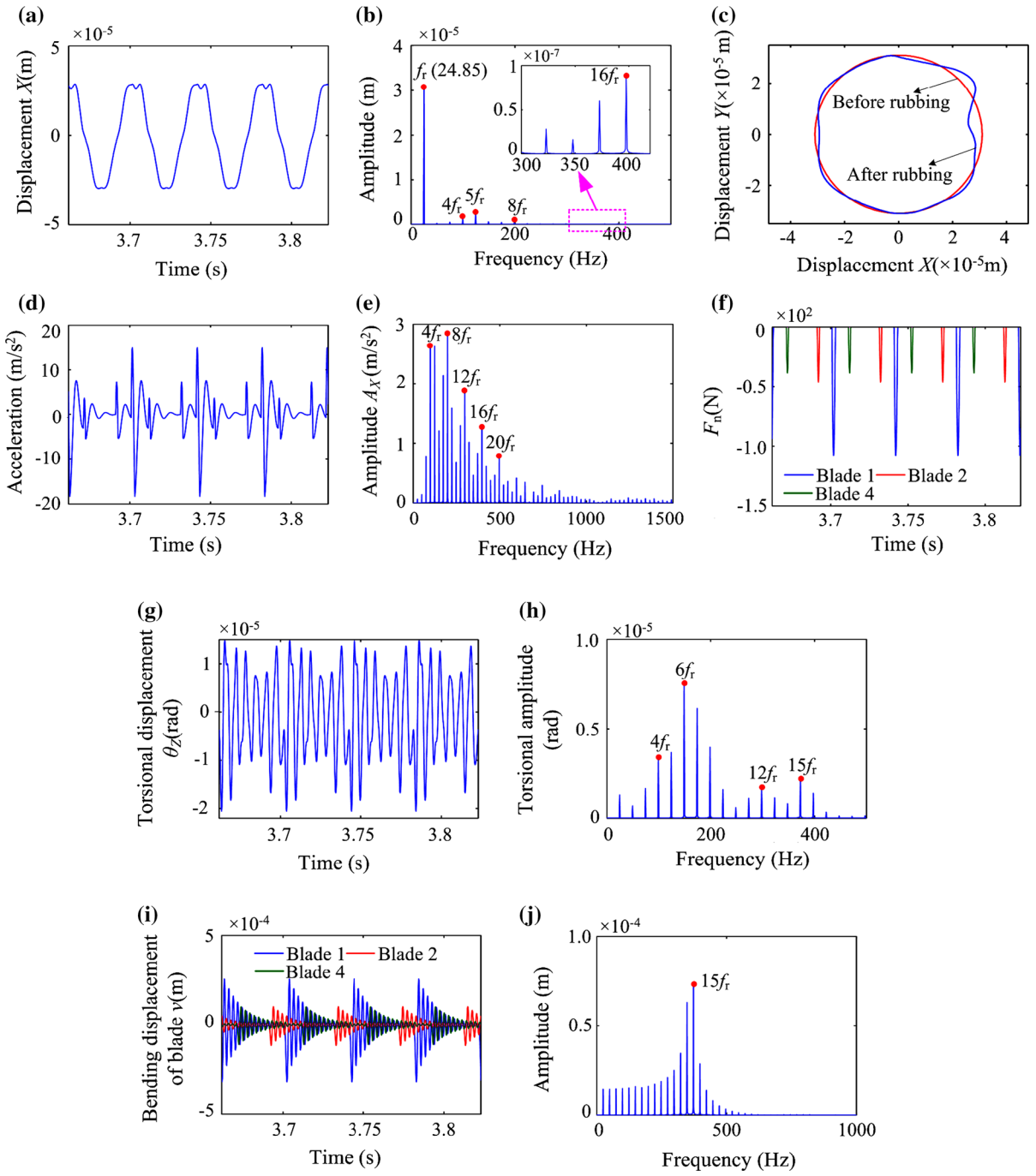

Fig. 18 Simulated results with four-blade rubbing (case 5): **a** rotor displacement waveform in X direction, **b** amplitude spectrum of the rotor in X direction, **c** rotor orbit, **d** acceleration waveform of casing in X direction, **e** amplitude spectrum of casing acceleration, **f** normal rubbing force, **g** torsional displacement waveform of the rotor, **h** torsional amplitude spectrum of the rotor, **i** bending displacements of the blades, **j** amplitude spectrum of bending displacements of the blade 1

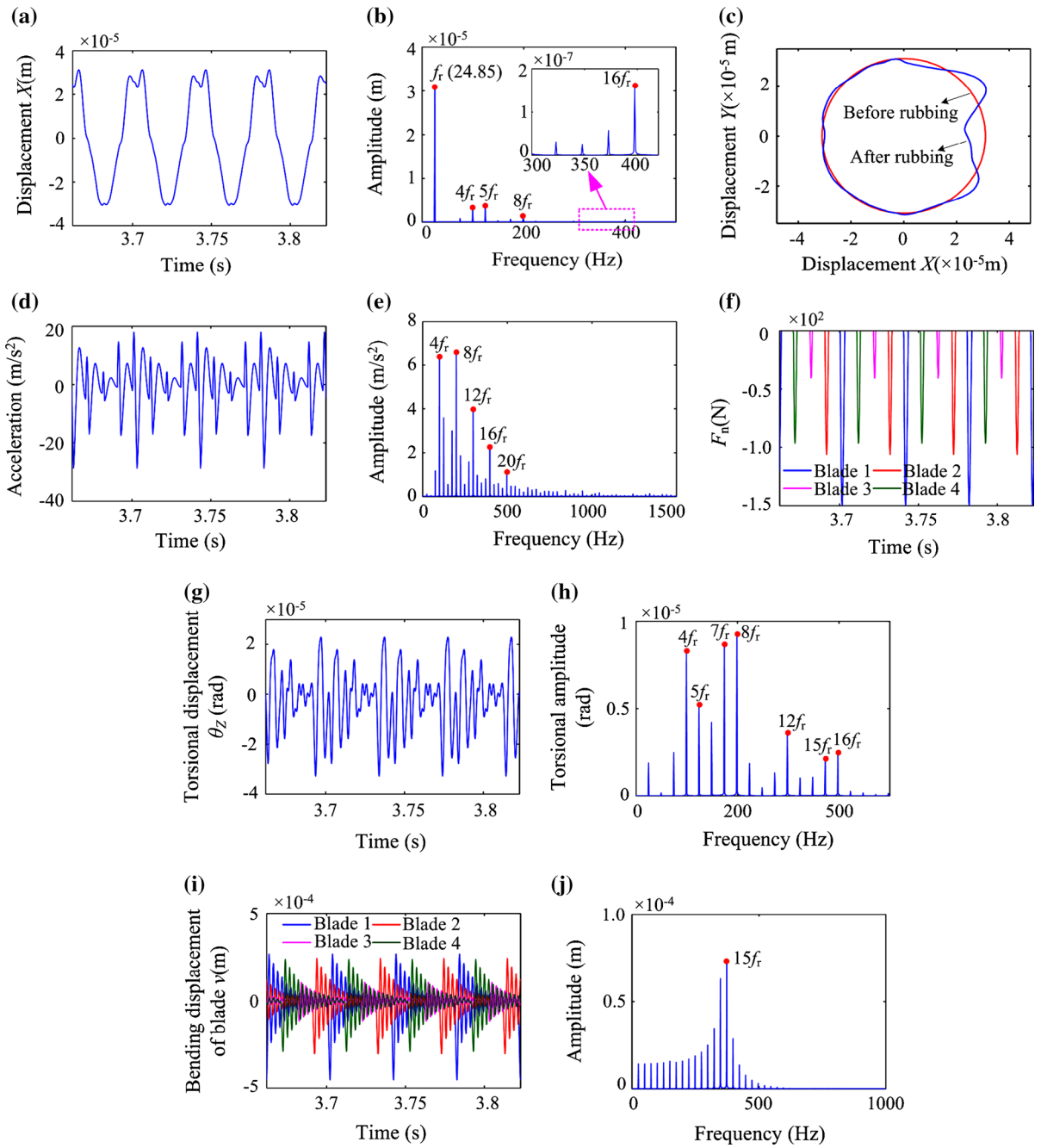

Fig. 19 Simulated results with four-blade rubbing under $\delta_0 = 80\mu$m: **a** rotor displacement waveform in X direction, **b** amplitude spectrum of the rotor in X direction, **c** rotor orbit, **d** acceleration waveform of casing in X direction, **e** amplitude spectrum of casing acceleration, **f** normal rubbing forces, **g** torsional displacement waveform of the rotor, **h** torsional amplitude spectrum of the rotor, **i** bending displacements of the blades, **j** amplitude spectrum of bending displacements of the blade 1

For single- and four-blade rubbings, measured results also show the similar amplitude amplification phenomena. Moreover, BPF and its multiple frequency components are also obvious for the four-blade rubbing. However, it should be noted that the amplitude spectra of the casing are complicated because the adopted casing

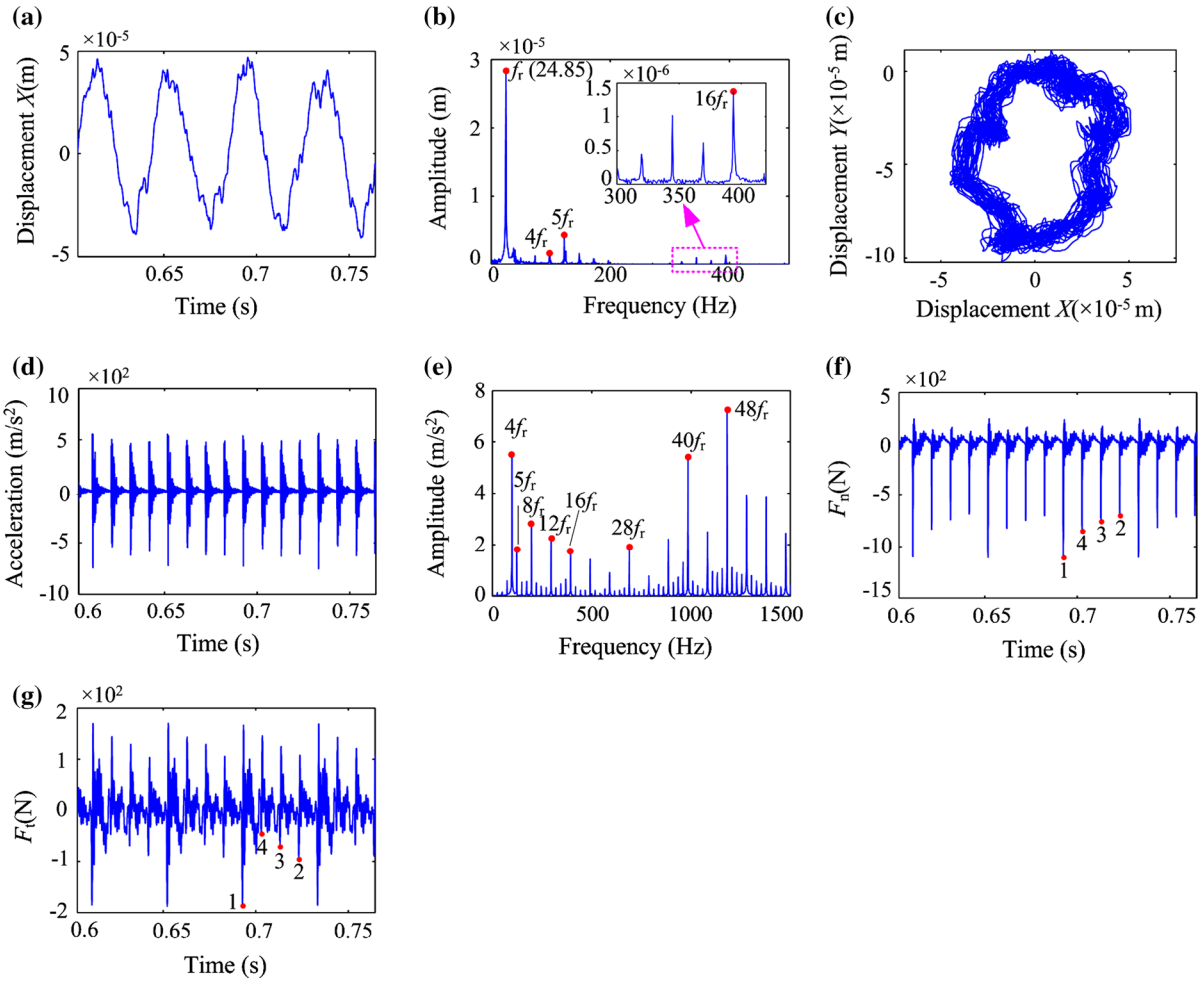

Fig. 20 Experimental results under case 5: **a** time-domain waveform of the rotor in *X* direction, **b** amplitude spectrum of the rotor, **c** rotor orbit, **d** time-domain waveform of the casing in *X* direction, **e** amplitude spectrum of the casing, **f** normal rubbing force, **g** tangential rubbing force. *Note* Numbers *1*, *4*, *3* and *2* denote the rubbing time for blades *1*, *4*, *3* and *2*

model is simple and it cannot completely simulate the dynamic characteristics of the actual casing structure.

5 Conclusions

An improved rotor-blade dynamic model is developed, and the model has some significant advantages compared with our previous model in [34]. In addition, the proposed model is also compared with finite element model [34], analytical models [34,35], and experiment results [34]. Then single- and four-blade rubbings are simulated by simplifying the casing as a lumped mass point with two degrees of freedom (DOFs). Finally, the simulated results are also validated using the experimental results. Main conclusions are summarized as follows:

(1) Compared with the model in Ref. [34], the proposed model considers the effects of the swing of the rigid disk and stagger angle of the blade. Natural frequencies of a flexible rotor-blade system obtained from the proposed model indicate that natural frequencies related to the disk swing are closer to those obtained from finite element (FE) model. For the case under study, the maximum percentage differences reduce from 3.934 % based on the ana-

Table 7 Fault features summary for single- and four-blade rubbings

Rubbing forms	Vibration forms	Fault features of simulated results	Fault features of measured results
Single-blade rubbing	Lateral vibration of the shaft	Amplification phenomena appear at the $8f_r$ (case 2) and $5f_r$ (case 3) near the conical natural frequencies	Amplification phenomena appear at the $8f_r$ (case 2) and $5f_r$ (case 3) near the conical natural frequencies
	Torsional vibration of the shaft	Amplification phenomena appear at the $10f_r$ (case 2) and $6f_r$ (case 3) near the torsional natural frequency	
	Casing vibration	Amplification phenomena appear at the $8f_r$ (case 2) and $5f_r$ (case 3) near the casing natural frequency	Amplification phenomena appear at the $7f_r$, $58f_r$ and $70f_r$ (case 2) and $5f_r$, $39f_r$ and $48f_r$ (case 3) near the casing natural frequencies
	Blade vibration	Amplification phenomena appear at the $22f_r$ (case 2) and $15f_r$ (case 3) near bending natural frequencies of the blades	
Four-blade rubbing	Lateral vibration of the shaft	Large amplitude can be observed at BPF, 2BPF and 3BPF for case 4, and at BPF, $5f_r$ and 2BPF for case 5	Large amplitude can be observed at BPF, 2BPF and 3BPF for case 4, and at BPF and $5f_r$ for case 5
	Torsional vibration of the shaft	Large amplitude can be observed at BPF, 2BPF, $9f_r$, 3BPF, 4BPF, 5BPF and 6BPF for case 4, and at BPF, $6f_r$, $7f_r$, 2BPF, 3BPF, $15f_r$ and 4BPF for case 5	
	Casing vibration	Large amplitude can be observed at BPF, 2BPF, 3BPF, 4BPF, 5BPF and 6BPF for cases 4 and 5	Large amplitude can be observed at BPF, 2BPF, 3BPF, 4BPF, 5BPF, 6BPF, 15BPF and 18BPF for case 4, and at BPF, 2BPF, 3BPF, 4BPF, 7BPF, 10BPF and 12BPF for case 5
	Blade vibration	Amplification phenomena appear at the $22f_r$ (case 4) and $15f_r$ (case 5) near bending natural frequencies of the blades	

BPF blade passing frequency, *nBPF n* times of BPF

lytic model [34] to 0.1042 % based on the proposed model.

In addition, the shaft is discretized using FE method rather than the lumped mass method, which makes the shaft modeling more general. Furthermore, the mode shapes of the rotor-blade systems can be also obtained from the proposed model, which is also a new development relative to the analytical model in Ref. [34].

(2) Simulated rubbing responses show a good agreement with the experimental results. For the single-blade rubbing, amplitude amplification phenomena appear when the multiple frequency of the rotational frequency (f_r) coincides with the conical and torsional natural frequencies of the rotor-blade system, the bending natural frequencies of the blades, and the natural frequencies of the casing. For the four-blade rubbing, the blade passing frequency (BPF, $4f_r$) and its multiple frequency components are also obvious besides these frequencies related to amplitude amplification phenomena.

(3) Rubbing levels of the blades are related to the rotor whirl. The most severe rubbing appears for the blade which locates at the right end of the whirl

orbit, i.e., is nearest to the casing. The least severe rubbing appears for the blade located at the left end of the whirl orbit, which is the opposite side for the most severe rubbing blade. The rubbing levels related to other two blades are moderate.

In this study, the casing is simulated as a two DOFs system and only the whole displacement of the casing is considered, and only the rotor vibration displacements are measured. In the future studies, more complicated casing models such as elastic ring models will be introduced in the system model, and the effects of stagger angles of blades on the rubbing will be considered, and the shaft torsional vibration and blade dynamic stress will also be measured.

Acknowledgments This project is supported by Program for the Joint Funds of the National Natural Science Foundation and the Civil Aviation Administration of China (Grant No. U1433109), the Fundamental Research Funds for the Central Universities (Grant Nos. N130403006 and N140301001) and the National Basic Research Program of China (Grant No. 2011CB706504) for providing financial support for this work. We also thank the anonymous reviewers for their valuable comments and Professor Ziqiang Lang and Dr. Yuzhu Guo from the University of Sheffield for the proof reading of the final version of the paper and offering suggestions on the improvement of presentation.

Conflict of interest The authors declare that there is no conflict of interests regarding the publication of this article.

Appendix 1: Vectors and matrices related to the blades

(1) $\boldsymbol{q}_\mathrm{b}$ is the generalized coordinates vector of the blades, where

$$\boldsymbol{q}_\mathrm{b} = \left[\begin{array}{cccc} \boldsymbol{q}_\mathrm{b}^1 & \cdots \boldsymbol{q}_\mathrm{b}^i \cdots & \boldsymbol{q}_\mathrm{b}^{N_\mathrm{b}} \end{array}\right]^\mathrm{T},$$
$$\boldsymbol{q}_\mathrm{b}^i = \left[\begin{array}{ccc} \boldsymbol{U}^{i\,\mathrm{T}} & \boldsymbol{V}^{i\,\mathrm{T}} & \boldsymbol{\psi}^{i\,\mathrm{T}} \end{array}\right]^\mathrm{T}, \tag{24}$$

here, $\boldsymbol{U}^i = [U_1^i, \ldots, U_{N_\mathrm{mod}}^i]^\mathrm{T}$, $\boldsymbol{V}^i = \left[V_1^i, \ldots, V_{N_\mathrm{mod}}^i\right]^\mathrm{T}$, $\boldsymbol{\psi}^i = \left[\psi_1^i, \ldots, \psi_{N_\mathrm{mod}}^i\right]^\mathrm{T}$.

(2) $\boldsymbol{M}_\mathrm{b}$ is the mass matrix of the blades

$$\boldsymbol{M}_\mathrm{b} = \mathrm{diag}[\,\boldsymbol{M}_\mathrm{b}^1 \quad \cdots \quad \boldsymbol{M}_\mathrm{b}^i \quad \cdots \quad \boldsymbol{M}_\mathrm{b}^{N_\mathrm{b}}\,], \tag{25}$$

where $\boldsymbol{M}_\mathrm{b}^i$ is the mass matrix of the ith blade, and the elements of $\boldsymbol{M}_\mathrm{b}^i$ are given as follows:

$$\boldsymbol{M}_\mathrm{b}^i(m,n) = \sum_{n=1}^{N_\mathrm{mod}} \left[\rho_\mathrm{b} \int_0^L A_\mathrm{b}\phi_{1n}\phi_{1m}\mathrm{d}x\right],$$
$$\boldsymbol{M}_\mathrm{b}^i\,(m+N_\mathrm{mod}, n+N_\mathrm{mod}) = \sum_{n=1}^{N_\mathrm{mod}} \left[\rho_\mathrm{b} \int_0^L A_\mathrm{b}\phi_{2n}\phi_{2m}\mathrm{d}x\right],$$
$$\boldsymbol{M}_\mathrm{b}^i\,(m+2N_\mathrm{mod}, n+2N_\mathrm{mod}) = \sum_{n=1}^{N_\mathrm{mod}} \left[\rho_\mathrm{b} \int_0^L I_\mathrm{b}\phi_{3m}\phi_{3n}\mathrm{d}x\right],$$

here, $m, n = \xi = 1, 2, \ldots, N_\mathrm{mod}$, and the surplus elements are all zero.

(3) $\boldsymbol{G}_\mathrm{b}$ is the Coriolis force matrix of the blade:

$$\boldsymbol{G}_\mathrm{b} = \mathrm{diag}[\,\boldsymbol{G}_\mathrm{b}^1 \quad \cdots \quad \boldsymbol{G}_\mathrm{b}^i \quad \cdots \quad \boldsymbol{G}_\mathrm{b}^{N_\mathrm{b}}\,], \tag{26}$$

where $\boldsymbol{G}_\mathrm{b}^i$ is the Coriolis force matrix of the ith blade, and the elements of $\boldsymbol{G}_\mathrm{b}^i$ are given as follows:

$$\boldsymbol{G}_\mathrm{b}^i\,(m, n+N_\mathrm{mod}) = \sum_{n=1}^{N_\mathrm{mod}} \left[-2\dot{\theta}\rho_\mathrm{b}\cos\beta \int_0^L A_\mathrm{b}\phi_{2n}\phi_{1m}\mathrm{d}x\right],$$
$$\boldsymbol{G}_\mathrm{b}^i\,(m+N_\mathrm{mod}, n) = \sum_{n=1}^{N_\mathrm{mod}} \left[2\dot{\theta}\rho_\mathrm{b}\cos\beta \int_0^L A_\mathrm{b}\phi_{1n}\phi_{2m}\mathrm{d}x\right],$$

and the surplus elements are all zero.

(4) $\boldsymbol{K}_\mathrm{b}$ is the stiffness matrix of the blades:

$$\boldsymbol{K}_\mathrm{b} = \mathrm{diag}\left[\,\boldsymbol{K}_\mathrm{b}^1 \quad \cdots \quad \boldsymbol{K}_\mathrm{b}^i \quad \cdots \quad \boldsymbol{K}_\mathrm{b}^{N_\mathrm{b}}\,\right], \tag{27}$$

where $\boldsymbol{K}_\mathrm{b}^i$ is the stiffness matrix of the ith blade, and the elements of $\boldsymbol{K}_\mathrm{b}^i$ are given as follows:

$$\boldsymbol{K}_\mathrm{b}^i(m,n) = \sum_{n=1}^{N_\mathrm{mod}} \left[-\dot{\theta}^2\rho_\mathrm{b}\int_0^L A_\mathrm{b}\phi_{1n}\phi_{1m}\mathrm{d}x + E_\mathrm{b}A_\mathrm{b}\phi_{1n}'\phi_{1m}\big|_{x=L} - \int_0^L E_\mathrm{b}\left(A_\mathrm{b}'\phi_{1n}' + A_\mathrm{b}\phi_{1n}''\right)\phi_{1m}\mathrm{d}x\right],$$
$$\boldsymbol{K}_\mathrm{b}^i\,(m, n+N_\mathrm{mod}) = \sum_{n=1}^{N_\mathrm{mod}} \left[-\ddot{\theta}\cos\beta\rho_\mathrm{b}\int_0^L A_\mathrm{b}\phi_{2n}\phi_{1m}\mathrm{d}x\right],$$
$$\boldsymbol{K}_\mathrm{b}^i\,(m+N_\mathrm{mod}, n) = \sum_{n=1}^{N_\mathrm{mod}} \left[\ddot{\theta}\cos\beta\rho_\mathrm{b}\int_0^L A_\mathrm{b}\phi_{1n}\phi_{2m}\mathrm{d}x\right],$$

$$\boldsymbol{K}_{\mathrm{b}}^{i}\left(m+N_{\mathrm{mod}},n+N_{\mathrm{mod}}\right)=\sum_{n=1}^{N_{\mathrm{mod}}}\begin{bmatrix}\kappa G_{\mathrm{b}}A_{\mathrm{b}}\phi_{2n}'\phi_{2m}\big|_{x=L}-\int_{0}^{L}\kappa G_{\mathrm{b}}\left(A_{\mathrm{b}}'\phi_{2n}'+A_{\mathrm{b}}\phi_{2n}''\right)\phi_{2m}\mathrm{d}x\\ +f_{\mathrm{c}}(x)\ \phi_{2n}'\phi_{2m}\big|_{x=L}-\int_{0}^{L}\left(f_{\mathrm{c}}'(x)\phi_{2n}'+f_{\mathrm{c}}(x)\phi_{2n}''\right)\phi_{2m}\mathrm{d}x\\ +F_{\mathrm{n}}\ \phi_{2n}'\phi_{2m}\big|_{x=L}-\int_{0}^{L}\left(F_{\mathrm{n}}\phi_{2n}''+F_{\mathrm{n}}'\phi_{2n}'\right)\phi_{2m}\mathrm{d}x-\dot{\theta}^{2}\cos^{2}\beta\rho_{\mathrm{b}}\int_{0}^{L}A_{\mathrm{b}}\phi_{2n}\phi_{2m}\mathrm{d}x\end{bmatrix},$$

$$\boldsymbol{K}_{\mathrm{b}}^{i}\left(m+N_{\mathrm{mod}},n+2N_{\mathrm{mod}}\right)=\sum_{n=1}^{N_{\mathrm{mod}}}\Big[-\kappa G_{\mathrm{b}}A_{\mathrm{b}}\phi_{3n}\phi_{2m}\big|_{x=L}+\int_{0}^{L}\kappa G_{\mathrm{b}}\left(A_{\mathrm{b}}'\phi_{3n}+A_{\mathrm{b}}\phi_{3n}'\right)\phi_{2m}\mathrm{d}x\Big],$$

$$\boldsymbol{K}_{\mathrm{b}}^{i}\left(m+2N_{\mathrm{mod}},n+N_{\mathrm{mod}}\right)=\sum_{n=1}^{N_{\mathrm{mod}}}\left[-\int_{0}^{L}\kappa G_{\mathrm{b}}A_{\mathrm{b}}\phi_{2n}'\phi_{3m}\mathrm{d}x\right],$$

$$\boldsymbol{K}_{\mathrm{b}}^{i}\left(m+2N_{\mathrm{mod}},n+2N_{\mathrm{mod}}\right)=\sum_{n=1}^{N_{\mathrm{mod}}}\begin{bmatrix}E_{\mathrm{b}}I_{\mathrm{b}}\phi_{3n}'\phi_{3m}\big|_{x=L}-\int_{0}^{L}E_{\mathrm{b}}\left(I_{\mathrm{b}}'\phi_{3n}'+I_{\mathrm{b}}\phi_{3n}''\right)\phi_{3m}\mathrm{d}x\\ +\int_{0}^{L}\kappa G_{\mathrm{b}}A_{\mathrm{b}}\phi_{3n}\phi_{3m}\mathrm{d}x-\dot{\theta}^{2}\rho_{\mathrm{b}}\int_{0}^{L}I_{\mathrm{b}}\phi_{3n}\phi_{3m}\mathrm{d}x\end{bmatrix},$$

and the surplus elements are all zero.

Appendix 2: Coupled vectors and matrices related to rotor-blade systems

Mass matrix

The mass coupling matrix of rotor-blade systems is

$$\boldsymbol{M}_{\mathrm{c}}=[\boldsymbol{M}_{\mathrm{c1}},\boldsymbol{M}_{\mathrm{c2}},\boldsymbol{M}_{\mathrm{c3}},\boldsymbol{M}_{\mathrm{c4}},\boldsymbol{M}_{\mathrm{c5}},\boldsymbol{M}_{\mathrm{c6}}]. \tag{28}$$

(1) $\boldsymbol{M}_{\mathrm{c1}}$ is the mass coupling term at the disk location in X direction.

$$\boldsymbol{M}_{\mathrm{c1}}=\begin{bmatrix}\boldsymbol{M}_{\mathrm{c1}}^{1} & \cdots & \boldsymbol{M}_{\mathrm{c1}}^{i} & \cdots & \boldsymbol{M}_{\mathrm{c1}}^{N_{\mathrm{b}}}\end{bmatrix}^{\mathrm{T}}, \tag{29}$$

where the superscript i denotes the ith blade. The elements of $\boldsymbol{M}_{\mathrm{c1}}^{i}$ are given as follows:

$$\boldsymbol{M}_{\mathrm{c1}}^{i}(m,1)=\rho_{\mathrm{b}}\cos\vartheta_{i}\int_{0}^{L}A_{\mathrm{b}}\phi_{1m}\mathrm{d}x,$$

$$\boldsymbol{M}_{\mathrm{c1}}^{i}(m+N_{\mathrm{mod}},1)=-\rho_{\mathrm{b}}\sin\vartheta_{i}\cos\beta\int_{0}^{L}A_{\mathrm{b}}\phi_{2m}\mathrm{d}x,$$

$$\boldsymbol{M}_{\mathrm{c1}}^{i}(m+2N_{\mathrm{mod}},1)=0.$$

(2) $\boldsymbol{M}_{\mathrm{c2}}$ is the mass coupling term at the disk location in Y direction.

$$\boldsymbol{M}_{\mathrm{c2}}=\begin{bmatrix}\boldsymbol{M}_{\mathrm{c2}}^{1} & \cdots & \boldsymbol{M}_{\mathrm{c2}}^{i} & \cdots & \boldsymbol{M}_{\mathrm{c2}}^{N_{\mathrm{b}}}\end{bmatrix}^{\mathrm{T}}. \tag{30}$$

The elements of $\boldsymbol{M}_{\mathrm{c2}}^{i}$ are given as follows:

$$\boldsymbol{M}_{\mathrm{c2}}^{i}(m,1)=\rho_{\mathrm{b}}\sin\vartheta_{i}\int_{0}^{L}A_{\mathrm{b}}\phi_{1m}\mathrm{d}x,$$

$$\boldsymbol{M}_{\mathrm{c2}}^{i}(m+N_{\mathrm{mod}},1)=\rho_{\mathrm{b}}\cos\vartheta_{i}\cos\beta\int_{0}^{L}A_{\mathrm{b}}\phi_{2m}\mathrm{d}x,$$

$$\boldsymbol{M}_{\mathrm{c2}}^{i}(m+2N_{\mathrm{mod}},1)=0.$$

(3) $\boldsymbol{M}_{\mathrm{c3}}$ is the mass coupling term at the disk location in Z direction.

$$\boldsymbol{M}_{\mathrm{c3}}=\begin{bmatrix}\boldsymbol{M}_{\mathrm{c3}}^{1} & \cdots & \boldsymbol{M}_{\mathrm{c3}}^{i} & \cdots & \boldsymbol{M}_{\mathrm{c3}}^{N_{\mathrm{b}}}\end{bmatrix}^{\mathrm{T}}. \tag{31}$$

The elements of $\boldsymbol{M}_{\mathrm{c3}}^{i}$ are given as follows:

$$\boldsymbol{M}_{\mathrm{c3}}^{i}(m,1)=0,$$

$$\boldsymbol{M}_{\mathrm{c3}}^{i}(m+N_{\mathrm{mod}},1)=\rho_{\mathrm{b}}\sin\beta\int_{0}^{L}A_{\mathrm{b}}\phi_{2m}\mathrm{d}x,$$

$$\boldsymbol{M}_{\mathrm{c3}}^{i}(m+2N_{\mathrm{mod}},1)=0.$$

(4) $\boldsymbol{M}_{c4}$ is the mass coupling term at the disk location in θ_X direction.

$$\boldsymbol{M}_{c4} = \left[\boldsymbol{M}_{c4}^{1} \quad \cdots \quad \boldsymbol{M}_{c4}^{i} \quad \cdots \quad \boldsymbol{M}_{c4}^{N_b} \right]^{T}. \quad (32)$$

The elements of $\boldsymbol{M}_{c4}^{i}$ are given as follows:

$$\begin{aligned}
&\boldsymbol{M}_{c4}^{i}(m, 1) = 0,\\
&\boldsymbol{M}_{c4}^{i}(m + N_{mod}, 1)\\
&\quad = \rho_b \sin\vartheta_i \sin\beta \int_0^L (R_d + x) A_b \phi_{2m} dx,\\
&\boldsymbol{M}_{c4}^{i}(m + 2N_{mod}, 1)\\
&\quad = \rho_b \sin\vartheta_i \sin\beta \int_0^L I_b \phi_{3m} dx.
\end{aligned}$$

(5) $\boldsymbol{M}_{c5}$ is the mass coupling term at the disk location in θ_Y direction.

$$\boldsymbol{M}_{c5} = \left[\boldsymbol{M}_{c5}^{1} \quad \cdots \quad \boldsymbol{M}_{c5}^{i} \quad \cdots \quad \boldsymbol{M}_{c5}^{N_b} \right]^{T}. \quad (33)$$

The elements of $\boldsymbol{M}_{c5}^{i}$ are given as follows:

$$\begin{aligned}
&\boldsymbol{M}_{c5}^{i}(m, 1) = 0,\\
&\boldsymbol{M}_{c5}^{i}(m + N_{mod}, 1)\\
&\quad = -\rho_b \cos\vartheta_i \sin\beta \int_0^L (R_d + x) A_b \phi_{2m} dx,\\
&\boldsymbol{M}_{c5}^{i}(m + 2N_{mod}, 1)\\
&\quad = -\rho_b \cos\vartheta_i \sin\beta \int_0^L I_b \phi_{3m} dx.
\end{aligned}$$

(6) $\boldsymbol{M}_{c6}$ is the mass coupling term at the disk location in θ_Z direction.

$$\boldsymbol{M}_{c6} = \left[\boldsymbol{M}_{c6}^{1} \quad \cdots \quad \boldsymbol{M}_{c6}^{i} \quad \cdots \quad \boldsymbol{M}_{c6}^{N_b} \right]^{T}. \quad (34)$$

The elements of $\boldsymbol{M}_{c6}^{i}$ are given as follows:

$$\begin{aligned}
&\boldsymbol{M}_{c6}^{i}(m, 1) = 0,\\
&\boldsymbol{M}_{c6}^{i}(m + N_{mod}, 1)\\
&\quad = \rho_b \cos\beta \int_0^L (R_d + x) A_b \phi_{2m} dx,\\
&\boldsymbol{M}_{c6}^{i}(m + 2N_{mod}, 1)\\
&\quad = \rho_b \cos\beta \int_0^L I_b \phi_{3m} dx.
\end{aligned}$$

Damping matrix

The damping coupling matrix of rotor-blade systems at the disk location is

$$\boldsymbol{G}_c = [\boldsymbol{G}_{c1}, \boldsymbol{G}_{c2}, \boldsymbol{G}_{c3}, \boldsymbol{G}_{c4}, \boldsymbol{G}_{c5}, \boldsymbol{G}_{c6}], \quad (35)$$

where $\boldsymbol{G}_{ci} = \boldsymbol{0}(i = 1, 2\ldots5)$, and the expression of $\boldsymbol{G}_{c6}$ is

$$\boldsymbol{G}_{c6} = \left[\boldsymbol{G}_{c6}^{1} \quad \cdots \quad \boldsymbol{G}_{c6}^{i} \quad \cdots \quad \boldsymbol{G}_{c6}^{N_b} \right]^{T}, \quad (36)$$

where the elements of $\boldsymbol{G}_{c6}^{i}$ are given as follows:

$$\begin{aligned}
&\boldsymbol{G}_{c6}^{i}(m, 1) = -2\dot{\theta}\rho_b \int_0^L A_b (R_d + x) \phi_{1m} dx,\\
&\boldsymbol{G}_{c6}^{i}(m + N_{mod}, 1) = 0,\\
&\boldsymbol{G}_{c6}^{i}(m + 2N_{mod}, 1) = 0.
\end{aligned}$$

Stiffness matrix

The stiffness coupling matrix of rotor-blade systems related to the acceleration at the disk location is

$$\boldsymbol{K}_{ac} = [\boldsymbol{K}_{ac1}, \boldsymbol{K}_{ac2}, \boldsymbol{K}_{ac3}, \boldsymbol{K}_{ac4}, \boldsymbol{K}_{ac5}, \boldsymbol{K}_{ac6}], \quad (37)$$

where $\boldsymbol{K}_{aci} = \boldsymbol{0}(i = 1, 2\ldots5)$, and the expression of $\boldsymbol{K}_{ac6}$ is

$$\boldsymbol{K}_{ac6} = \left[\boldsymbol{K}_{ac6}^{1} \quad \cdots \quad \boldsymbol{K}_{ac6}^{i} \quad \cdots \quad \boldsymbol{K}_{ac6}^{N_b} \right]^{T}. \quad (38)$$

The elements of $\boldsymbol{K}_{ac6}^{i}$ are given as follows:

$$\begin{aligned}
&\boldsymbol{K}_{ac6}^{i}(m, 1) = -\ddot{\theta}\rho_b \int_0^L A_b (R_d + x) \phi_{1m} dx,\\
&\boldsymbol{K}_{ac6}^{i}(m + N_{mod}, 1) = 0,\\
&\boldsymbol{K}_{ac6}^{i}(m + 2N_{mod}, 1) = 0.
\end{aligned}$$

The stiffness coupling matrix of rotor-blade systems is

$$\boldsymbol{K}_c = [\boldsymbol{K}_{c1}, \boldsymbol{K}_{c2}, \boldsymbol{K}_{c3}, \boldsymbol{K}_{c4}, \boldsymbol{K}_{c5}, \boldsymbol{K}_{c6}], \quad (39)$$

where $\boldsymbol{K}_{ci} = \boldsymbol{0}(i = 1, 2\ldots5)$, and the expression of $\boldsymbol{K}_{c6}$ is

$$\boldsymbol{K}_{c6} = \left[\boldsymbol{K}_{c6}^{1} \quad \cdots \quad \boldsymbol{K}_{c6}^{i} \quad \cdots \quad \boldsymbol{K}_{c6}^{N_b} \right]^{T}. \quad (40)$$

The elements of $\boldsymbol{K}_{c6}^{i}$ are given as follows:

$$\begin{aligned}
&\boldsymbol{K}_{c6}^{i}(m, 1) = 0,\\
&\boldsymbol{K}_{c6}^{i}(m + N_{mod}, 1) = -\dot{\theta}^2 \cos\beta\rho_b \int_0^L A_b (R_d + x) \phi_{2m} dx,\\
&\boldsymbol{K}_{c6}^{i}(m + 2N_{mod}, 1) = -\dot{\theta}^2 \cos\beta\rho_b \int_0^L I_b \phi_{3m} dx.
\end{aligned}$$

Appendix 3: Other vectors and matrices related to the rotor-blade system

(1) $\tilde{\boldsymbol{M}}_d$ is the added mass matrix at the disk location.

$$\tilde{\boldsymbol{M}}_{\mathrm{d}}=\begin{bmatrix}\tilde{M}_{XX} & 0 & 0 & 0 & 0 & \tilde{M}_{X\theta_Z}\\ 0 & \tilde{M}_{YY} & 0 & 0 & 0 & \tilde{M}_{Y\theta_Z}\\ 0 & 0 & \tilde{M}_{ZZ} & \tilde{M}_{Z\theta_X} & \tilde{M}_{Z\theta_Y} & 0\\ 0 & 0 & \tilde{M}_{\theta_X Z} & \tilde{M}_{\theta_X\theta_X} & \tilde{M}_{\theta_X\theta_Y} & \tilde{M}_{\theta_X\theta_Z}\\ 0 & 0 & \tilde{M}_{\theta_Y Z} & \tilde{M}_{\theta_Y\theta_X} & \tilde{M}_{\theta_Y\theta_Y} & \tilde{M}_{\theta_Y\theta_Z}\\ \tilde{M}_{\theta_Z X} & \tilde{M}_{\theta_Z Y} & 0 & \tilde{M}_{\theta_Z\theta_X} & \tilde{M}_{\theta_Z\theta_Y} & \tilde{M}_{\theta_Z\theta_Z}\end{bmatrix}, \tag{41}$$

where, $\tilde{M}_{XX}=\sum_{i=1}^{N_\mathrm{b}}\int_0^L\rho_\mathrm{b}A_\mathrm{b}\mathrm{d}x$, $\tilde{M}_{YY}=\sum_{i=1}^{N_\mathrm{b}}\int_0^L\rho_\mathrm{b}A_\mathrm{b}\mathrm{d}x$, $\tilde{M}_{ZZ}=\sum_{i=1}^{N_\mathrm{b}}\int_0^L\rho_\mathrm{b}A_\mathrm{b}\mathrm{d}x$,

$$\tilde{M}_{\theta_X\theta_X}=\sum_{i=1}^{N_\mathrm{b}}\left(\sin^2\vartheta_i\int_0^L\rho_\mathrm{b}A_\mathrm{b}\,(R_\mathrm{d}+x)^2\mathrm{d}x+\sin^2\beta\int_0^L\rho_\mathrm{b}I_\mathrm{b}\mathrm{d}x+\cos^2\vartheta_i\cos^2\beta\int_0^L\rho_\mathrm{b}I_\mathrm{b}\mathrm{d}x\right),$$

$$\tilde{M}_{\theta_Y\theta_Y}=\sum_{i=1}^{N_\mathrm{b}}\left(\cos^2\vartheta_i\int_0^L\rho_\mathrm{b}A_\mathrm{b}\,(R_\mathrm{d}+x)^2\mathrm{d}x+\sin^2\beta\int_0^L\rho_\mathrm{b}I_\mathrm{b}\mathrm{d}x+\sin^2\vartheta_i\cos^2\beta\int_0^L\rho_\mathrm{b}I_\mathrm{b}\mathrm{d}x\right),$$

$$\tilde{M}_{\theta_Z\theta_Z}=m_\mathrm{d}e^2+\sum_{i=1}^{N_\mathrm{b}}\left(\int_0^L\rho_\mathrm{b}A_\mathrm{b}\,(R_\mathrm{d}+x)^2\mathrm{d}x+\int_0^L\rho_\mathrm{b}I_\mathrm{b}\cos^2\beta\mathrm{d}x\right),$$

$$\tilde{M}_{X\theta_Z}=\tilde{M}_{\theta_Z X}=\sum_{i=1}^{N_\mathrm{b}}\int_0^L-\rho_\mathrm{b}A_\mathrm{b}\,(R_\mathrm{d}+x)\sin\vartheta_i\mathrm{d}x,$$

$$\tilde{M}_{Y\theta_Z}=\tilde{M}_{\theta_Z Y}=\sum_{i=1}^{N_\mathrm{b}}\int_0^L\rho_\mathrm{b}A_\mathrm{b}\,(R_\mathrm{d}+x)\cos\vartheta_i\mathrm{d}x,$$

$$\tilde{M}_{Z\theta_X}=\tilde{M}_{\theta_X Z}=\sum_{i=1}^{N_\mathrm{b}}\int_0^L\rho_\mathrm{b}A_\mathrm{b}\,(R_\mathrm{d}+x)\sin\vartheta_i\mathrm{d}x,$$

$$\tilde{M}_{Z\theta_Y}=\tilde{M}_{\theta_Y Z}=\sum_{i=1}^{N_\mathrm{b}}\int_0^L-\rho_\mathrm{b}A_\mathrm{b}\,(R_\mathrm{d}+x)\cos\vartheta_i\mathrm{d}x,$$

$$\tilde{M}_{\theta_X\theta_Y}=\tilde{M}_{\theta_Y\theta_X}=\sum_{i=1}^{N_\mathrm{b}}\left(\int_0^L-\rho_\mathrm{b}A_\mathrm{b}\,(R_\mathrm{d}+x)^2\sin\vartheta_i\cos\vartheta_i\mathrm{d}x+\int_0^L\rho_\mathrm{b}I_\mathrm{b}\sin\vartheta_i\cos\vartheta_i\cos^2\beta\mathrm{d}x\right),$$

$$\tilde{M}_{\theta_X\theta_Z}=\tilde{M}_{\theta_Z\theta_X}=\sum_{i=1}^{N_\mathrm{b}}\int_0^L\rho_\mathrm{b}I_\mathrm{b}\sin\vartheta_i\sin\beta\cos\beta\mathrm{d}x,$$

$$\tilde{M}_{\theta_Y\theta_Z}=\tilde{M}_{\theta_Z\theta_Y}=\sum_{i=1}^{N_\mathrm{b}}\int_0^L-\rho_\mathrm{b}I_\mathrm{b}\cos\vartheta_i\sin\beta\cos\beta\mathrm{d}x.$$

(2) $\tilde{\boldsymbol{G}}_\mathrm{d}$ is the added damping matrix at the disk location.

$$\tilde{\boldsymbol{G}}_\mathrm{d}=\begin{bmatrix}0&0&0&0&0&0\\0&0&0&0&0&0\\0&0&0&0&0&0\\0&0&0&\tilde{G}_{\theta_X\theta_X}&\tilde{G}_{\theta_X\theta_Y}&0\\0&0&0&\tilde{G}_{\theta_Y\theta_X}&\tilde{G}_{\theta_Y\theta_Y}&0\\0&0&0&0&0&0\end{bmatrix}, \tag{42}$$

where $\tilde{G}_{\theta_X\theta_X}=\sum_{i=1}^{N_\mathrm{b}}\left(2\dot{\theta}\sin\vartheta_i\cos\vartheta_i\int_0^L\rho_\mathrm{b}A_\mathrm{b}\,(R_\mathrm{d}+x)^2\,\mathrm{d}x-2\dot{\theta}\sin\vartheta_i\cos\vartheta_i\cos^2\beta\int_0^L\rho_\mathrm{b}I_\mathrm{b}\mathrm{d}x\right)$,

$$\tilde{G}_{\theta_Y\theta_Y}=\sum_{i=1}^{N_\mathrm{b}}\left(-2\dot{\theta}\sin\vartheta_i\cos\vartheta_i\int_0^L\rho_\mathrm{b}A_\mathrm{b}\,(R_\mathrm{d}+x)^2\mathrm{d}x+2\dot{\theta}\sin\vartheta_i\cos\vartheta_i\cos^2\beta\int_0^L\rho_\mathrm{b}I_\mathrm{b}\mathrm{d}x\right),$$

$$\tilde{G}_{\theta_X\theta_Y}=\sum_{i=1}^{N_\mathrm{b}}\left(2\dot{\theta}\sin^2\vartheta_i\int_0^L\rho_\mathrm{b}A_\mathrm{b}\,(R_\mathrm{d}+x)^2\mathrm{d}x+2\dot{\theta}\cos^2\vartheta_i\cos^2\beta\int_0^L\rho_\mathrm{b}I_\mathrm{b}\mathrm{d}x\right),$$

$$\tilde{G}_{\theta_Y\theta_X}=\sum_{i=1}^{N_\mathrm{b}}\left(-2\dot{\theta}\cos^2\vartheta_i\int_0^L\rho_\mathrm{b}A_\mathrm{b}\,(R_\mathrm{d}+x)^2\mathrm{d}x-2\dot{\theta}\sin^2\vartheta_i\cos^2\beta\int_0^L\rho_\mathrm{b}I_\mathrm{b}\mathrm{d}x\right).$$

(3) $\tilde{K}_\mathrm{d}$ is the added stiffness matrix at the disk location.

$$\tilde{K}_\mathrm{d}=\begin{bmatrix}0&0&0&0&0&0\\0&0&0&0&0&0\\0&0&0&0&0&0\\0&0&0&\tilde{K}_{\theta_X\theta_X}&\tilde{K}_{\theta_X\theta_Y}&0\\0&0&0&\tilde{K}_{\theta_Y\theta_X}&\tilde{K}_{\theta_Y\theta_Y}&0\\0&0&0&0&0&\tilde{K}_{\theta_Z\theta_Z}\end{bmatrix}, \tag{43}$$

where

$$\tilde{K}_{\theta_X\theta_X} = \sum_{i=1}^{N_b} \left(\begin{array}{l} \left(\ddot{\theta}\sin\vartheta_i\cos\vartheta_i - \dot{\theta}^2\sin^2\vartheta_i\right)\int_0^L \rho_b A_b\,(R_d+x)^2 \mathrm{d}x \\ +\left(-\ddot{\theta}\sin\vartheta_i\cos\vartheta_i\cos^2\beta - \dot{\theta}^2\cos^2\vartheta_i\cos^2\beta\right)\int_0^L \rho_b I_b \mathrm{d}x \end{array} \right),$$

$$\tilde{K}_{\theta_Y\theta_Y} = \sum_{i=1}^{N_b} \left(\begin{array}{l} \left(-\ddot{\theta}\sin\vartheta_i\cos\vartheta_i - \dot{\theta}^2\cos^2\vartheta_i\right)\int_0^L \rho_b A_b\,(R_d+x)^2 \mathrm{d}x \\ +\left(\ddot{\theta}\sin\vartheta_i\cos\vartheta_i\cos^2\beta - \dot{\theta}^2\sin^2\vartheta_i\cos^2\beta\right)\int_0^L \rho_b I_b \mathrm{d}x \end{array} \right),$$

$$\tilde{K}_{\theta_X\theta_Y} = \sum_{i=1}^{N_b} \left(\begin{array}{l} \left(\ddot{\theta}\sin^2\vartheta_i + \dot{\theta}^2\sin\vartheta_i\cos\vartheta_i\right)\int_0^L \rho_b A_b\,(R_d+x)^2 \mathrm{d}x \\ +\left(\ddot{\theta}\cos^2\vartheta_i\cos^2\beta - \dot{\theta}^2\sin\vartheta_i\cos\vartheta_i\cos^2\beta\right)\int_0^L \rho_b I_b \mathrm{d}x \end{array} \right),$$

$$\tilde{K}_{\theta_Y\theta_X} = \sum_{i=1}^{N_b} \left(\begin{array}{l} \left(-\ddot{\theta}\cos^2\vartheta_i + \dot{\theta}^2\sin\vartheta_i\cos\vartheta_i\right)\int_0^L \rho_b A_b\,(R_d+x)^2 \mathrm{d}x \\ -\left(\ddot{\theta}\sin^2\vartheta_i\cos^2\beta + \dot{\theta}^2\sin\vartheta_i\cos\vartheta_i\cos^2\beta\right)\int_0^L \rho_b I_b \mathrm{d}x \end{array} \right),$$

$$\tilde{K}_{\theta_Z\theta_Z} = \sum_{i=1}^{N_b} \left(-\int_0^L \rho_b A_b\,(R_d+x)^2\,\dot{\theta}^2 \mathrm{d}x - \int_0^L \rho_b I_b \dot{\theta}^2 \cos^2\beta \mathrm{d}x \right).$$

Appendix 4: Element matrices of the rotational shaft

The element consistent mass matrix of Timoshenko beam $\boldsymbol{M}^e$ is

$$\boldsymbol{M}^e = \rho A_s l \begin{bmatrix} a & & & & & & & & & & & \\ 0 & a & & & & & & & & & & \\ 0 & 0 & 1/3 & & & & & & & & & \\ 0 & -c & 0 & g & & & & & & & & \\ c & 0 & 0 & 0 & g & & & & & & & \\ 0 & 0 & 0 & 0 & 0 & J/(3A_s) & & & & & & \\ b & 0 & 0 & 0 & d & 0 & a & & & & & \\ 0 & b & 0 & -d & 0 & 0 & 0 & a & & & & \\ 0 & 0 & 1/6 & 0 & 0 & 0 & 0 & 0 & 1/3 & & & \\ 0 & d & 0 & f & 0 & 0 & 0 & c & 0 & g & & \\ -d & 0 & 0 & 0 & f & 0 & -c & 0 & 0 & 0 & g & \\ 0 & 0 & 0 & 0 & 0 & J/(6A_s) & 0 & 0 & 0 & 0 & 0 & J/(3A_s) \end{bmatrix}, \quad (44)$$

Symmetric

where

$$a = \frac{\frac{13}{35} + \frac{7}{10}\phi + \frac{1}{3}\phi^2 + \frac{6}{5}(r_g/l)^2}{(1+\phi)^2},$$

$$b = \frac{\frac{9}{70} + \frac{3}{10}\phi + \frac{1}{6}\phi^2 - \frac{6}{5}(r_g/l)^2}{(1+\phi)^2},$$

$$c = \frac{\left[\frac{11}{210} + \frac{11}{120}\phi + \frac{1}{24}\phi^2 + \left(\frac{1}{10} - \frac{1}{2}\phi\right)(r_g/l)^2\right] l}{(1+\phi)^2},$$

$$d = \frac{\left[\frac{13}{420} + \frac{3}{40}\phi + \frac{1}{24}\phi^2 - \left(\frac{1}{10} - \frac{1}{2}\phi\right)(r_g/l)^2\right] l}{(1+\phi)^2},$$

$$f = \frac{\left[\frac{1}{140} + \frac{1}{60}\phi + \frac{1}{120}\phi^2 + \left(\frac{1}{30} + \frac{1}{6}\phi - \frac{1}{6}\phi^2\right)(r_g/l)^2\right] l^2}{(1+\phi)^2},$$

$$g = \frac{\left[\frac{1}{105} + \frac{1}{60}\phi + \frac{1}{120}\phi^2 + \left(\frac{2}{15} + \frac{1}{6}\phi + \frac{1}{3}\phi^2\right)(r_g/l)^2\right] l^2}{(1+\phi)^2},$$

in which the transverse shear parameter $\phi = \frac{12EI}{\kappa_1 A_s G l^2}$; I is the area moment of inertia; $\kappa_1 = \frac{6(1+\upsilon)}{7+6\upsilon}$ is the shape of factor; A_s is the shaft cross-sectional area; G is shear modulus; l is element length; J is polar area moment of inertia; the radius of gyration $r_g = \sqrt{I/A_s}$.

Element stiffness matrix of Timoshenko beam $\boldsymbol{K}^e$ is

$$\boldsymbol{K}^{\mathrm{e}}=\begin{bmatrix} h & & & & & & & & & & & \\ 0 & h & & & & & & & & & & \\ 0 & 0 & A_sE/l & & & & & & & & & \\ 0 & -i & 0 & j & & & & & & & & \\ i & 0 & 0 & 0 & j & & & & & & & \\ 0 & 0 & 0 & 0 & 0 & GJ/l & & & & & & \\ -h & 0 & 0 & 0 & -i & 0 & h & & & & & \\ 0 & -h & 0 & i & 0 & 0 & 0 & h & & & & \\ 0 & 0 & -A_sE/l & 0 & 0 & 0 & 0 & 0 & A_sE/l & & & \\ 0 & -i & 0 & k & 0 & 0 & 0 & i & 0 & j & & \\ i & 0 & 0 & 0 & k & 0 & -i & 0 & 0 & 0 & j & \\ 0 & 0 & 0 & 0 & 0 & -GJ/l & 0 & 0 & 0 & 0 & 0 & GJ/l \end{bmatrix}, \quad \text{Symmetric} \tag{45}$$

where $h=\frac{12EI}{l^3(1+\phi)}$, $i=\frac{6EI}{l^2(1+\phi)}$, $j=\frac{(4+\phi)EI}{l(1+\phi)}$ and $k=\frac{(2-\phi)EI}{l(1+\phi)}$.

Gyroscopic matrix of Timoshenko beam $\boldsymbol{G}^{\mathrm{e}}$ is

$$\boldsymbol{G}^{\mathrm{e}}=2\dot{\theta}\rho A_s l\begin{bmatrix} 0 & & & & & & & & & & & \\ -p & 0 & & & & & & & & & & \\ 0 & 0 & 0 & & & & & & & & & \\ -q & 0 & 0 & 0 & & & & & & & & \\ 0 & -q & 0 & -s & 0 & & & & & & & \\ 0 & 0 & 0 & 0 & 0 & 0 & & & & & & \\ 0 & -p & 0 & -q & 0 & 0 & 0 & & & & & \\ p & 0 & 0 & 0 & -q & 0 & -p & 0 & & & & \\ 0 & 0 & 0 & 0 & 0 & 0 & 0 & 0 & 0 & & & \\ -q & 0 & 0 & 0 & w & 0 & q & 0 & 0 & 0 & & \\ 0 & -q & 0 & -w & 0 & 0 & 0 & q & 0 & -s & 0 & \\ 0 & 0 & 0 & 0 & 0 & 0 & 0 & 0 & 0 & 0 & 0 & 0 \end{bmatrix}, \quad \text{Antisymmetric} \tag{46}$$

where $p=\frac{6r_g^2/5}{l^2(1+\phi)^2}$, $q=\frac{-\left(\frac{1}{10}-\frac{1}{2}\phi\right)r_g^2}{l(1+\phi)^2}$, $s=\frac{\left(\frac{2}{15}+\frac{1}{6}\phi+\frac{1}{3}\phi^2\right)r_g^2}{(1+\phi)^2}$ and $w=\frac{-\left(\frac{1}{30}+\frac{1}{6}\phi-\frac{1}{6}\phi^2\right)r_g^2}{(1+\phi)^2}$.

Appendix 5: Nonlinear forces of the rotor-blade system

(1) $\boldsymbol{F}^i_{\text{nonlinear, b}}$ is a nonlinear force vector of ith blade:

$$\boldsymbol{F}^i_{\text{nonlinear, b}}(m,1)=\dot{\theta}^2\rho_{\mathrm{b}}\int_0^L(R_{\mathrm{d}}+x)\,\phi_{1m}A_{\mathrm{b}}\mathrm{d}x,$$

$$\boldsymbol{F}^i_{\text{nonlinear, b}}(m+N_{\mathrm{mod}},1)=\begin{pmatrix} -\ddot{\theta}\cos\beta \\ -2\sin\vartheta_i\sin\beta\dot{\theta}_{Y\mathrm{d}}\dot{\theta}-\sin\vartheta_i\sin\beta\theta_{Y\mathrm{d}}\ddot{\theta} \\ -\cos\vartheta_i\sin\beta\theta_{Y\mathrm{d}}\dot{\theta}^2-2\cos\vartheta_i\sin\beta\dot{\theta}_{X\mathrm{d}}\dot{\theta} \\ -\cos\vartheta_i\sin\beta\theta_{X\mathrm{d}}\ddot{\theta}+\sin\vartheta_i\sin\beta\theta_{X\mathrm{d}}\dot{\theta}^2 \end{pmatrix}$$

$$\rho_{\mathrm{b}}\int_0^L A_{\mathrm{b}}(R_{\mathrm{d}}+x)\,\phi_{2m}\mathrm{d}x, \tag{47}$$

$$\boldsymbol{F}^i_{\text{nonlinear,b}}(m+2N_{\mathrm{mod}},1)=-\ddot{\theta}\cos\beta\rho_{\mathrm{b}}\int_0^L I_{\mathrm{b}}\phi_{3m}\mathrm{d}x. \tag{48}$$

(2) $f_{\text{nonlinear},X}$ is a nonlinear force applied on the disk in X direction.

$$
\begin{aligned}
f_{\text{nonlinear, }X} &= em_{\text{d}}\cos\left(\theta+\theta_{Z\text{d}}\right)\left(\dot{\theta}+\dot{\theta}_{Z\text{d}}\right)^2 \\
&+em_{\text{d}}\sin\left(\theta+\theta_{Z\text{d}}\right)\left(\ddot{\theta}+\ddot{\theta}_{Z\text{d}}\right) \\
&+\sum_{i=1}^{N_{\text{b}}}\sum_{i=1}^{N_{\text{mod}}}\left(\begin{array}{l} 2\dot{\theta}\sin\vartheta_i\int_0^L \rho_{\text{b}}A_{\text{b}}\phi_{1m}\dot{U}_m\text{d}x \\ +\left(\dot{\theta}^2\cos\vartheta_i+\ddot{\theta}\sin\vartheta_i\right)\int_0^L \rho_{\text{b}}A_{\text{b}}\phi_{1m}U_m\text{d}x \end{array}\right) \\
&+\sum_{i=1}^{N_{\text{b}}}\sum_{i=1}^{N_{\text{mod}}}\left(\begin{array}{l} 2\dot{\theta}\cos\vartheta_i\cos\beta\int_0^L \rho_{\text{b}}A_{\text{b}}\phi_{2m}\dot{V}_m\text{d}x \\ +\left(-\dot{\theta}^2\sin\vartheta_i+\ddot{\theta}\cos\vartheta_i\right)\cos\beta\int_0^L \rho_{\text{b}}A_{\text{b}}\phi_{2m}V_m\text{d}x \end{array}\right) \\
&+\sum_{i=1}^{N_{\text{b}}}\left(\left(\begin{array}{l} 2\dot{\theta}_{Z\text{d}}\dot{\theta}\cos\vartheta_i-\theta_{Z\text{d}}\dot{\theta}^2\sin\vartheta_i+\theta_{Z\text{d}}\ddot{\theta}\cos\vartheta_i \\ +\dot{\theta}^2\cos\vartheta_i+\ddot{\theta}\sin\vartheta_i \end{array}\right)\right. \\
&\left.\int_0^L \rho_{\text{b}}A_{\text{b}}\left(R_{\text{d}}+x\right)\text{d}x\right).
\end{aligned}
\tag{49}
$$

(3) $f_{\text{nonlinear},Y}$ is a nonlinear force applied on the disk in Y direction.

$$
\begin{aligned}
f_{\text{nonlinear},Y} &= em_{\text{d}}\sin\left(\theta+\theta_{Z\text{d}}\right)\left(\dot{\theta}+\dot{\theta}_{Z\text{d}}\right)^2 \\
&-em_{\text{d}}\cos\left(\theta+\theta_{Z\text{d}}\right)\left(\ddot{\theta}+\ddot{\theta}_{Z\text{d}}\right) \\
&+\sum_{i=1}^{N_{\text{b}}}\sum_{i=1}^{N_{\text{mod}}}\left(\begin{array}{l} -2\dot{\theta}\cos\vartheta_i\int_0^L \rho_{\text{b}}A_{\text{b}}\phi_{1m}\dot{U}_m\text{d}x \\ +\left(\dot{\theta}^2\sin\vartheta_i-\ddot{\theta}\cos\vartheta_i\right)\int_0^L \rho_{\text{b}}A_{\text{b}}\phi_{1m}U_m\text{d}x \end{array}\right) \\
&+\sum_{i=1}^{N_{\text{b}}}\sum_{i=1}^{N_{\text{mod}}}\left(\begin{array}{l} 2\dot{\theta}\sin\vartheta_i\cos\beta\int_0^L \rho_{\text{b}}A_{\text{b}}\phi_{2m}\dot{V}_m\text{d}x \\ +\left(\dot{\theta}^2\cos\vartheta_i+\ddot{\theta}\sin\vartheta_i\right)\cos\beta\int_0^L \rho_{\text{b}}A_{\text{b}}\phi_{2m}V_m\text{d}x \end{array}\right) \\
&+\sum_{i=1}^{N_{\text{b}}}\left(\left(\begin{array}{l} 2\dot{\theta}_{z\text{d}}\dot{\theta}\sin\vartheta_i+\theta_{Z\text{d}}\dot{\theta}^2\cos\vartheta_i+\theta_{Z\text{d}}\ddot{\theta}\sin\vartheta_i \\ +\dot{\theta}^2\sin\vartheta_i-\ddot{\theta}\cos\vartheta_i \end{array}\right)\right. \\
&\left.\int_0^L \rho_{\text{b}}A_{\text{b}}\left(\text{R}_{\text{d}}+x\right)\text{d}x\right).
\end{aligned}
\tag{50}
$$

(4) $f_{\text{nonlinear},Z}$ is a nonlinear force applied on the disk in Z direction.

$$
\begin{aligned}
f_{\text{nonlinear},Z} = \sum_{i=1}^{N_{\text{b}}}&\left(\left(\begin{array}{l} -2\dot{\theta}_{Y\text{d}}\dot{\theta}\sin\vartheta_i-\theta_{Y\text{d}}\ddot{\theta}\sin\vartheta_i-\theta_{Y\text{d}}\dot{\theta}^2\cos\vartheta_i \\ -2\dot{\theta}_{X\text{d}}\dot{\theta}\cos\vartheta_i-\theta_{X\text{d}}\ddot{\theta}\cos\vartheta_i+\theta_{X\text{d}}\dot{\theta}^2\sin\vartheta_i \end{array}\right)\right. \\
&\left.\int_0^L \rho_{\text{b}}A_{\text{b}}\left(\text{R}_{\text{d}}+x\right)\text{d}x\right).
\end{aligned}
\tag{51}
$$

(5) $M_{\text{nonlinear},X}$ is a nonlinear bending moment applied on the disk in θ_{X} direction.

$$
\begin{aligned}
&M_{\text{nonlinear},\,X} = -J_p\dot{\theta}_{Y\text{d}}\dot{\theta}_{Z\text{d}} \\
&+\sum_{i=1}^{N_\text{b}}\left(\begin{pmatrix} -2\dot{\theta}_{Z\text{d}}\dot{\theta}\cos\vartheta_i - \theta_{Z\text{d}}\ddot{\theta}\cos\vartheta_i \\ +\theta_{Z\text{d}}\dot{\theta}^2\sin\vartheta_i - \ddot{\theta}\sin\vartheta_i - \dot{\theta}^2\cos\vartheta_i \end{pmatrix}\right. \\
&\left.\sin\beta\cos\beta\int_0^L \rho_\text{b} I_\text{b}\mathrm{d}x\right) \\
&+\sum_{i=1}^{N_\text{b}}\sum_{i=1}^{N_\text{mod}} \\
&\times\begin{pmatrix} -2\dot{\theta}\cos\vartheta_i\sin\beta\int_0^L \rho_\text{b} I_\text{b}\phi_{3\text{m}}\dot{\psi}_\text{m}\mathrm{d}x \\ +\left(-\ddot{\theta}\cos\vartheta_i + \dot{\theta}^2\sin\vartheta_i\right)\sin\beta\int_0^L \rho_\text{b} I_\text{b}\phi_{3\text{m}}\psi_\text{m}\mathrm{d}x \end{pmatrix}
\end{aligned}
\tag{52}
$$

(6) $M_{\text{nonlinear},Y}$ is a nonlinear bending moment applied on the disk in θ_{Y} direction.

$$
\begin{aligned}
&M_{\text{nonlinear},\,Y} = J_p\left(\ddot{\theta}\theta_{X\text{d}} + \ddot{\theta}_{Z\text{d}}\theta_{X\text{d}} + \dot{\theta}_{Z\text{d}}\dot{\theta}_{X\text{d}}\right) \\
&+\sum_{i=1}^{N_\text{b}}\left(\begin{pmatrix} -2\dot{\theta}_{Z\text{d}}\dot{\theta}\sin\vartheta_i - \theta_{Z\text{d}}\ddot{\theta}\sin\vartheta_i \\ -\theta_{Z\text{d}}\dot{\theta}^2\cos\vartheta_i + \ddot{\theta}\cos\vartheta_i - \dot{\theta}^2\sin\vartheta_i \end{pmatrix}\right. \\
&\left.\sin\beta\cos\beta\int_0^L \rho_\text{b} I_\text{b}\mathrm{d}x\right) \\
&+\sum_{i=1}^{N_\text{b}}\sum_{i=1}^{N_\text{mod}} \\
&\times\begin{pmatrix} -2\dot{\theta}\sin\vartheta_i\sin\beta\int_0^L \rho_\text{b} I_\text{b}\phi_{3\text{m}}\dot{\psi}_\text{m}\mathrm{d}x \\ +\left(-\ddot{\theta}\sin\vartheta_i - \dot{\theta}^2\cos\vartheta_i\right)\sin\beta\int_0^L \rho_\text{b} I_\text{b}\phi_{3\text{m}}\psi_\text{m}\mathrm{d}x \end{pmatrix}
\end{aligned}
\tag{53}
$$

.

(7) $M_{\text{nonlinear},Z}$ is a nonlinear torque applied on the disk in θz direction.

$$
\begin{aligned}
&M_{\text{nonlinear},\,Z} = em_\text{d}\sin\left(\theta+\theta_{Z\text{d}}\right)\ddot{X}_\text{d} \\
&-em_\text{d}\cos\left(\theta+\theta_{Z\text{d}}\right)\ddot{Y}_\text{d} - e^2 m_\text{d}\ddot{\theta} - J_\text{p}\ddot{\theta} \\
&+J_p\left(\dot{\theta}_{X\text{d}}\dot{\theta}_{Y\text{d}} + \theta_{X\text{d}}\ddot{\theta}_{Y\text{d}}\right) \\
&-\sum_{i=1}^{N_\text{b}}\left(\ddot{\theta}\rho_\text{b}\int_0^L \left(A_\text{b}\left(R_\text{d}+x\right)^2 + I_\text{b}\cos^2\beta\right)\mathrm{d}x\right).
\end{aligned}
\tag{54}
$$

References

1. Jacquet-Richardet, G., Torkhani, M., Cartraud, P., et al.: Rotor to stator contacts in turbomachines. Review and application. Mech. Syst. Signal Pr. **40**, 401–420 (2013)
2. Muszynska, A.: Rotor to stationary element rub-related vibration phenomena in rotating machinery-literature survey. Shock Vib. Digest **21**, 3–11 (1989)
3. Jiang, J., Chen, Y.H.: Advances in the research on nonlinear phenomena in rotor/stator rubbing systems. Adv. Mech. **43**, 132–148 (2013). (in Chinese)
4. Leong, M.S.: Field experiences of gas turbines vibrations—a review and case studies. J. Syst. Des. Dyn. **2**, 24–35 (2008)
5. Legrand, M., Pierre, C., Peseux, B.: Structural modal interaction of a four degree of freedom bladed disk and casing model. J. Comput. Nonlinear. Dyn. **5**, 13–41 (2010)
6. Legrand, M., Pierre, C., Cartraud, P., et al.: Two-dimensional modeling of an aircraft engine structural bladed disk-casing modal interaction. J. Sound Vib. **319**, 366–391 (2009)
7. Lesaffre, N., Sinou, J.J., Thouverez, F.: Stability analysis of rotating beams rubbing on an elastic circular structure. J. Sound Vib. **299**, 1005–1032 (2007)
8. Sinha, S.K.: Non-linear dynamic response of a rotating radial Timoshenko beam with periodic pulse loading at the free-end. Int. J. Nonlinear. Mech. **40**, 113–149 (2005)
9. Sinha, S.K.: Combined torsional-bending-axial dynamics of a twisted rotating cantilever Timoshenko beam with contact-impact loads at the free end. J. Appl. Mech. **74**, 505–522 (2007)
10. Kou, H.J., Yuan, H.Q.: Rub-induced non-linear vibrations of a rotating large deflection plate. Int. J. Nonlinear. Mech. **58**, 283–294 (2014)
11. Yuan, H.Q., Kou, H.J.: Contact-impact analysis of a rotating geometric nonlinear plate under thermal shock. J. Eng. Math. **90**, 119–140 (2015)
12. Almeida, P., Gibert, G., Thouverez, F., et al.: On some physical phenomena involved in blade-casing contact. In: Proceedings of the 9th International Conference on Structural Dynamics, EURODYN 2014, Porto, Portugal, 30 June–2 July (2014)
13. Batailly, A., Meingast, M., Legrand, M.: Unilateral contact induced blade/casing vibratory interactions in impellers: analysis for rigid casings. J. Sound Vib. **337**, 244–262 (2015)
14. Ma, H., Tai, X.Y., Han, Q.K., et al.: A revised model for rubbing between rotating blade and elastic casing. J. Sound Vib. **337**, 301–320 (2015)
15. Ma, H., Wang, D., Tai, X.Y., et al.: Vibration response analysis of blade-disk dovetail structure under blade tip rubbing condition. J. Vib. Control (2015). doi:10.1177/1077546315575835
16. Salvat, N., Batailly, A., Legrand, M.: Two-dimensional modeling of shaft precessional motions induced by blade/casing unilateral contact in aircraft engines. In: ASME Turbo Expo 2014: Turbine Technical Conference and Exposition, American Society of Mechanical Engineers (2014)
17. Kascak, A.F., Tomko, J. J.: Effects of Different Rub Models on Simulated Rotor Dynamics. NASA Technical Paper 2220 (1984)
18. Padovan, J., Choy, F.K.: Nonlinear dynamics of rotor/blade/casing rub interactions. J. Turbomach. **109**, 527–534 (1987)
19. Lawrence, C., Carney, K., Gallardo, V.: A Study of Fan Stage/Casing Interaction Models. National Aeronautics and Space Administration, Glenn Research Center, NASA/TM–2003-212215 (2003)
20. Sinha, S.K.: Dynamic characteristics of a flexible bladed-rotor with Coulomb damping due to tip-rub. J. Sound Vib. **273**, 875–919 (2004)

21. Sinha, S.K.: Rotordynamic analysis of asymmetric turbofan rotor due to fan blade-loss event with contact-impact rub loads. J. Sound Vib. **332**, 2253–2283 (2013)
22. Lesaffre, N., Sinou, J.J., Thouverez, F.: Contact analysis of a flexible bladed-rotor. Eur. J. Mech. A-Solid. **26**, 541–557 (2007)
23. Parent, M., Thouverez, F., Chevillot, F.: Whole engine interaction in a bladed rotor-to-stator contact. In: Proceedings of ASME Turbo Expo 2014: Turbine Technical Conference and Exposition, American Society of Mechanical Engineers (2014)
24. Parent, M., Thouverez, F., Chevillot F.: 3D interaction in bladed rotor-to-stator contact. In: Proceedings of the 9th International Conference on Structural Dynamics, EURODYN 2014, Porto, Portugal, 30 June–2 July (2014)
25. Ma, H., Tai, X.Y., Niu, H.Q., et al.: Numerical research on rub-impact fault in a blade-rotor-casing coupling system. J. Vibroeng. **15**, 1477–1489 (2013)
26. Petrov E.: Multiharmonic analysis of nonlinear whole engine dynamics with bladed disc-casing rubbing contacts. In: ASME Turbo Expo 2012: Turbine Technical Conference and Exposition, American Society of Mechanical Engineers (2012)
27. Thiery, F., Gustavsson, R., Aidanpaa, J.O.: Dynamics of a misaligned Kaplan turbine with blade-to-stator contacts. Int. J. Mech. Sci. **99**, 251–261 (2015)
28. Ahrens, J., Ulbrich, H., Ahaus, G.: Measurement of contact forces during blade rubbing. In: Vibrations in Rotating Machinery, 7th International Conference, Nottingham, pp. 259–268. ImechE, London (2000)
29. Padova, C., Barton, J., Dunn, M.G., et al.: Development of an experimental capability to produce controlled blade tip/shroud rubs at engine speed. J. Turbomach. **127**, 726–735 (2005)
30. Padova, C., Barton, J., Dunn, M.G., et al.: Experimental results from controlled blade tip/shroud rubs at engine speed. J. Turbomach. **129**, 713–723 (2007)
31. Chen, G., Liu, Y.Q., Jiang, G.Y., et al.: A novel method for identifying rotor-stator rubbing positions using the cepstrum analysis technique. J. Mech. Sci. Technol. **28**, 3537–3544 (2014)
32. Lim, M.H., Leong, M.S.: Detection of early faults in rotating machinery based on wavelet analysis. Adv. Mech. Eng. **2013**, 1–8 (2013)
33. Abdelrhman, A.M., Leong, M.S., Hee, L.M., et al.: Application of wavelet analysis in blade faults diagnosis for multi-stages rotor system. Appl. Mech. Mater. **393**, 959–964 (2013)
34. Ma, H., Lu, Y., Wu, Z.Y., et al.: A new dynamic model of rotor-blade systems. J. Sound Vib. **357**, 168–194 (2015)
35. Yang, C.H., Huang, S.C.: Coupling vibrations in rotating shaft-disk-blades system. J. Vib. Acoust. **129**, 48–57 (2007)